






Predictions for measuring the 21-cm multifrequency angular power spectrum using SKA-Low

Rajesh Mondal ¹★, Abinash Kumar Shaw ², Ilian T. Iliev ¹, Somnath Bharadwaj,²
Kanan K. Datta,³ Suman Majumdar ^{4,5}, Anjan K. Sarkar⁶ and Keri L. Dixon ⁷

¹*Astronomy Centre, Department of Physics and Astronomy, University of Sussex, Brighton BN19QH, UK*

²*Department of Physics & Centre for Theoretical Studies, Indian Institute of Technology Kharagpur, Kharagpur 721302, India*

³*Department of Physics, Presidency University, 86/1 College Street, Kolkata 700073, India*

⁴*Discipline of Astronomy, Astrophysics and Space Engineering, Indian Institute of Technology Indore, Simrol, Indore 453552, India*

⁵*Department of Physics, Blackett Laboratory, Imperial College, London SW7 2AZ, UK*

⁶*Astronomy & Astrophysics Group, Raman Research Institute, Bengaluru 560080, India*

⁷*New York University Abu Dhabi, Saadiyat Island, Abu Dhabi PO Box 129188, United Arab Emirates*

Accepted 2020 April 9. Received 2020 April 6; in original form 2019 October 11

ABSTRACT

The light-cone effect causes the mean as well as the statistical properties of the redshifted 21-cm signal $T_b(\hat{n}, \nu)$ to change with frequency ν (or cosmic time). Consequently, the statistical homogeneity (ergodicity) of the signal along the line-of-sight (LoS) direction is broken. This is a severe problem particularly during the Epoch of Reionization (EoR) when the mean neutral hydrogen fraction (\bar{x}_{HI}) changes rapidly as the Universe evolves. This will also pose complications for large bandwidth observations. These effects imply that the 3D power spectrum $P(k)$ fails to quantify the entire second-order statistics of the signal as it assumes the signal to be ergodic and periodic along the LoS. As a proper alternative to $P(k)$, we use the multifrequency angular power spectrum (MAPS) $C_\ell(\nu_1, \nu_2)$, which does not assume the signal to be ergodic and periodic along the LoS. Here, we study the prospects for measuring the EoR 21-cm MAPS using future observations with the upcoming SKA-Low. Ignoring any contribution from the foregrounds, we find that the EoR 21-cm MAPS can be measured at a confidence level $\geq 5\sigma$ at angular scales $\ell \sim 1300$ for total observation time $t_{\text{obs}} \geq 128$ h across ~ 44 MHz observational bandwidth. We also quantitatively address the effects of foregrounds on MAPS detectability forecast by avoiding signal contained within the foreground wedge in $(\mathbf{k}_\perp, k_\parallel)$ plane. These results are very relevant for the upcoming large bandwidth EoR experiments as previous predictions were all restricted to individually analysing the signal over small frequency (or equivalent redshift) intervals.

Key words: methods: statistical – techniques: interferometric – cosmology: theory – dark ages, reionization, first stars – diffuse radiation – large-scale structure of Universe.

1 INTRODUCTION

The Epoch of Reionization (EoR) is one of the important periods in the evolutionary history of our Universe. During this epoch, the ionizing radiation from the first luminous sources in the Universe gradually ionizes the neutral Hydrogen (HI) in the intergalactic medium (IGM). As more and more of these sources form, the ionized (H II) regions grow and eventually overlap and fill almost the entire IGM. Our present knowledge about this epoch is very limited. The current measurements of the Thomson scattering optical depth

(Planck Collaboration XLVI, XLVII 2016a, b), a measure of the line-of-sight (LoS) free electron opacity to cosmic microwave background (CMB) radiation in the IGM, suggest that the mean neutral fraction \bar{x}_{HI} falls by ~ 0.1 at $z \sim 10$ from a completely neutral IGM. The second observation is the Gunn–Peterson optical depth of the high-redshift quasar spectra (Becker et al. 2001; Fan et al. 2002, 2006; Becker et al. 2015). These measurements show an absorption trough at $z \lesssim 6$, which indicates that the IGM was neutral at 0.1 per cent level by $z \sim 6$. The third and the most recent constraint comes from the measurements of the luminosity function and clustering properties of high- z Lyman α emitters (Konno et al. 2014; Santos, Sobral & Matthee 2016; Ota et al. 2017; Zheng et al. 2017). These studies indicate a patchy distribution of HI and infer a

* E-mail: rajeshmondal18@gmail.com; Rajesh.Mondal@sussex.ac.uk

sharp increase in $\bar{x}_{\text{H I}}$ at redshifts larger than $z \sim 7$. The findings of all these indirect observations provide an overall indication that the EoR probably extends over a redshift range $6 \lesssim z \lesssim 12$ (Robertson et al. 2013, 2015; Mitra, Choudhury & Ferrara 2015, 2017; Dai et al. 2019). However, these indirect observations are not able to shed light on various fundamental issues, such as the exact duration and timing of reionization, properties of the ionizing sources, the topology of H I at different cosmic times, etc.

Observations of the redshifted 21-cm signal caused by the hyperfine transition of H I in the IGM is the most promising probe of the EoR (Scott & Rees 1990; Bharadwaj & Sethi 2001). There has been a considerable observational effort devoted to measuring the EoR 21-cm signal using the presently operating radio interferometers e.g. the GMRT¹ (Paciga et al. 2013), LOFAR² (van Haarlem et al. 2013; Yatawatta et al. 2013), the MWA³ (Jacobs et al. 2016), and PAPER⁴ (Parsons et al. 2014; Ali et al. 2015; Jacobs et al. 2015). The presently operating (first-generation) radio interferometers are not sensitive enough to make tomographic images of the EoR 21-cm signal and can only make a statistical detection of the signal. Observing the EoR 21-cm signal is one of the major scientific goals of the upcoming radio telescopes e.g. SKA⁵ (Mellema et al. 2013; Koopmans et al. 2015) and HERA⁶ (DeBoer et al. 2017). These observations are very challenging due to the presence of foregrounds, system noise, and other calibration errors. Foregrounds are ~ 4 – 5 orders of magnitude stronger than the expected signal (Ali, Bharadwaj & Chengalur 2008; Bernardi et al. 2009; Ghosh et al. 2012; Paciga et al. 2013), and modelling or removing them from the actual data is more complicated. However, in this work, we assume the idealistic scenario where foregrounds can be removed completely.

The upcoming SKA-Low will have 512 stations,⁷ and each of them will be ~ 35 m in diameter. These stations will consist of several log-periodic dipole antennas. The telescope will also have ~ 20 deg² field of view, a compact core and three spiral arms that will extend up to ~ 60 km. SKA-Low will have enough sensitivity over a large range of frequencies (frequency band of 50–350 MHz) to image the EoR 21-cm signal (Mellema et al. 2015). Unlike the CMB, we can map the large-scale structure (LSS) of the universe in 3D using the redshifted 21-cm signal, with the third dimension being frequency (or cosmic time or redshift). However, one has to be very careful while quantifying the EoR 21-cm signal as the mean, as well as other statistical properties of the signal change with varying frequency or redshift due to the light-cone (LC) effect (Barkana & Loeb 2006; Datta et al. 2012; La Plante et al. 2014; Zawada et al. 2014; Mondal, Bharadwaj & Datta 2018).

The LC effect breaks the statistical homogeneity (ergodicity) along the LoS direction. Moreover, the main assumption that goes into the estimation of the power spectrum $P(k)$ or equivalently into the 3D Fourier transform is that the signal is ergodic and periodic. As a consequence of this fundamental difference between the assumption for Fourier transform and the actual properties of the signal, the spherically averaged 3D power spectrum $P(k)$ fails to quantify the entire second-order statistics of the signal (Mondal

et al. 2018) and gives a rather biased estimation of the signal (Trott 2016). This is particularly severe during the EoR when the $\bar{x}_{\text{H I}}$ changes rapidly as the reionization proceeds. This will also pose complications for broad bandwidth observations with SKA-Low (Mondal et al. 2019). The issue here is ‘how to quantify the statistics of the EoR 21-cm signal in the presence of the LC effect’. As a proper alternative to $P(k)$, we use the multifrequency angular power spectrum (MAPS) $C_\ell(\nu_1, \nu_2)$ (Datta, Choudhury & Bharadwaj 2007; Mondal et al. 2018, 2019), which does not assume ergodicity and periodicity along the LoS. The only assumption is that the EoR 21-cm signal is statistically homogeneous and isotropic in different directions on the sky plane. The visibilities are the main observables in every radio interferometric observations and the MAPS is directly associated with these visibility correlations. Therefore, it is relatively easy to estimate MAPS from the observations (Bharadwaj & Ali 2005; Ali et al. 2008; Ghosh et al. 2011).

Several studies have been made to quantify the sensitivity for measuring the EoR 21-cm power spectrum with different instruments (Morales 2005; McQuinn et al. 2006; Zaroubi et al. 2012; Beardsley et al. 2013; Pober et al. 2014; Ewall-Wice et al. 2016; Shaw, Bharadwaj & Mondal 2019). These predictions were restricted to individually analysing over small redshift (or equivalent frequency) intervals where they have worked with the 3D power spectrum $P(k)$. However, there is no such restriction for the MAPS, and we can, in principle, consider the entire bandwidth for the analysis. Here, we have made the signal-to-noise ratio (SNR) predictions for measuring the EoR 21-cm MAPS using future observations with SKA-Low. We have presented our results mainly considering a scenario, the ‘Optimistic’, where the observed MAPS is a sum of the EoR 21-cm MAPS and the system noise MAPS, ignoring any contribution from the foregrounds to the observed signal. However, we have also demonstrated the effects of foregrounds on the detection of the EoR 21-cm MAPS incorporating the foreground ‘wedge’. Note that we have used numerical simulations for computing the EoR 21-cm MAPS in our analysis.

The paper is structured as follows. In Section 2, we briefly describe the simulations used to generate the EoR 21-cm LC. Starting from the basic definition of the MAPS, we derive the expressions for the noise MAPS and MAPS error covariance in Section 3. In Section 5, we report the results i.e. the estimated MAPS, MAPS error covariance, and SNR assuming no foregrounds. Next, we discuss the impact of foregrounds on the prospects of detecting the 21-cm MAPS in Section 6. Finally, in Section 7, we summarize our results and conclude. Throughout the paper, we have used the values of cosmological parameters $\Omega_{\text{m}0} = 0.27$, $\Omega_{\Lambda 0} = 0.73$, $\Omega_{\text{b}0} h^2 = 0.02156$, $h = 0.7$, $\sigma_8 = 0.8$, and $n_s = 0.9619$. These values are consistent with the latest results from WMAP (Komatsu et al. 2011) and Planck combined with other available constraints (Planck Collaboration XIII, XLVII 2015, 2016b).

2 SIMULATING THE EOR 21-CM SIGNAL

2.1 The simulation

The density fields and halo catalogues are obtained from a high-resolution, large-volume N -body PRACE4LOFAR simulation (Giri et al. 2019). This simulation was run using the CUBEP³M code (Harnois-Deraps et al. 2013) and followed 6912³ particles in a comoving $500 h^{-1} \text{Mpc} \approx 714 \text{Mpc}$ per side volume to enable reliable halo identification (with 25 particles or more) down to $10^9 M_\odot$. The reionization process is simulated using the C²-RAY code (Mellema et al. 2006) on a 300³ grid with sources and density

¹<http://www.gmrt.ncra.tifr.res.in>

²<http://www.lofar.org>

³<http://www.mwatelescope.org>

⁴<http://eor.berkeley.edu>

⁵<http://www.skatelescope.org>

⁶<http://reionization.org>

⁷SKA1_LowConfigurationCoordinates-1.pdf

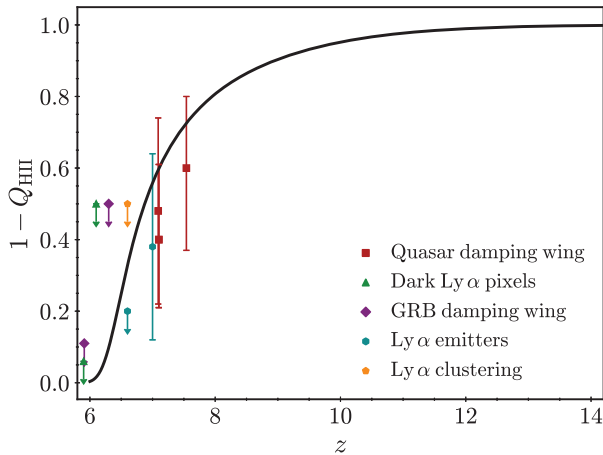


Figure 1. The reionization history as a function of redshift obtained from our simulation.

fields based on the N -body data following the method presented in Iliev et al. (2007) and Dixon et al. (2016). Specifically, for this work, we have used the data from the 714Mpc_g0.87_gS_300 reionization simulation following the notation of Dixon et al. (2016). We refer the reader to cited papers for details of the notation and set-up, with only a brief summary provided here.

The density fields are calculated using smoothed particle hydrodynamics-like smoothing. The sources of ionization are associated with the resolved haloes or high-mass atomically cooling haloes (HMACHs). These haloes are complemented by a subgrid model for the low-mass atomically cooling haloes (LMACHs) $10^8 < M_{\text{halo}} < 10^9$ (Ahn et al. 2015). Below this range, haloes are assumed to not form stars. For a source with halo mass M and lifetime t_s , we assign ionizing photon emissivity according to

$$\dot{N}_\gamma = g_\gamma \frac{M \Omega_b}{\mu m_p (10 \text{ Myr}) \Omega_0}, \quad (1)$$

where the efficiency g_γ combines the ionizing photon production efficiency of the stars per stellar atom, N_i , the star formation efficiency, f_* , and the escape fraction, f_{esc} :

$$g_\gamma = f_* f_{\text{esc}} N_i \left(\frac{10 \text{ Myr}}{t_s} \right) \quad (2)$$

(e.g. Haiman & Holder 2003; Iliev et al. 2012). The high-mass sources ($M > 10^9 M_\odot$) are assumed unaffected by the radiative feedback and assigned an efficiency $g_{\gamma, \text{HMACH}} = 0.87$. Prior to local reionization, the low-mass sources share the same efficiency as the high-mass sources. After the local ionization threshold exceeds 0.1, the low-mass sources have a mass-dependent efficiency

$$g_{\gamma, \text{LMACH}} \propto g_{\gamma, \text{HMACH}} \times \left[\frac{M}{9 \times 10^8 M_\odot} - \frac{1}{9} \right]. \quad (3)$$

We have generated the coeval brightness temperature (δT_b) cubes at 125 different redshifts in the range $6 \leq z < 16$, and the resulting reionization history is shown in Fig. 1. Our results are compared to observational inferences from Ly α damping wings (squares; Greig et al. 2017; Davies et al. 2018; Greig, Mesinger & Bañados 2019), dark Ly α forest pixels (triangles; McGreer, Mesinger & Fan 2011; McGreer, Mesinger & D’Odorico 2015), GRB damping wing absorption (diamonds; McQuinn et al. 2008; Chornock et al. 2013), decline in Ly α emitters (hexagons; Ota et al. 2008; Ouchi et al. 2010), and Ly α clustering (pentagons; Ouchi et al. 2010).

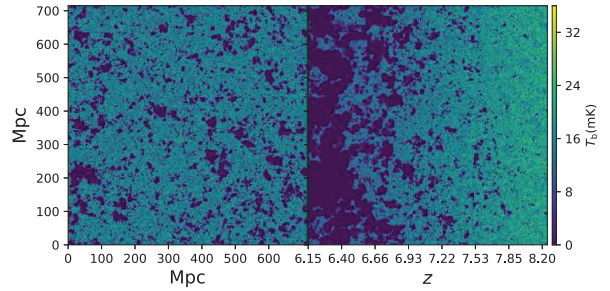


Figure 2. This shows sections through the 3D 21-cm brightness temperature maps for the coeval (left) and LC (right) simulations. The boxes are centred at redshift 7.09, which corresponds to the comoving distance $r_c = 8865.64$ Mpc and $\bar{x}_{\text{H I}} \approx 0.50$.

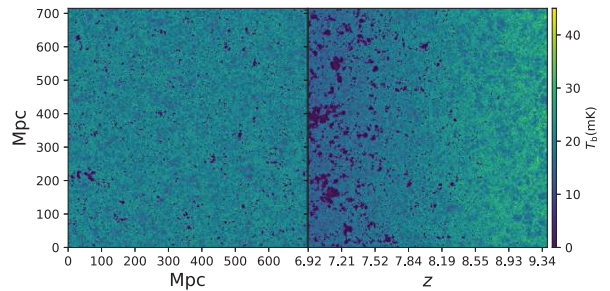


Figure 3. Same as Fig. 2 centred at redshift 8.04, which corresponds to the comoving distance $r_c = 9162.06$ Mpc and $\bar{x}_{\text{H I}} \approx 0.75$.

2.2 Generating the light-cones

We have generated our LCs following the formalism presented in Datta et al. (2014), using the simulated coeval δT_b cubes described in Section 2.1. We have generated two LCs: **LC1** centred at $z_c = 7.09$ (frequency $\nu_c = 175.58$ MHz), which corresponds to $\bar{x}_{\text{H I}} \approx 0.50$ and **LC2** centred at $z_c = 8.04$ ($\nu_c = 157.08$ MHz), which corresponds to $\bar{x}_{\text{H I}} \approx 0.75$. LC1 spans the redshift range $6.15 \lesssim z \lesssim 8.25$, which corresponds to change in the mass-averaged H I fraction $\bar{x}_{\text{H I}}$ (from end-to-end of the LC, following the reionization history shown in Fig. 1) as $\Delta \bar{x}_{\text{H I}} \approx 0.79 - 0.02 = 0.77$. Whereas, LC2 spans the range $6.92 \lesssim z \lesssim 9.40$, which corresponds to change in the $\bar{x}_{\text{H I}}$ as $\Delta \bar{x}_{\text{H I}} \approx 0.90 - 0.42 = 0.48$. Note that the redshift ranges, channel widths, and central frequencies assumed in the LCs are only representative values and may change. We have chosen these to observe the behaviour at two different stages of reionization history.

The right-hand panels of Figs 2 and 3 show sections through the simulated LC 21-cm brightness temperature maps. As a comparison, the left-hand panels of Figs 2 and 3 show the sections through coeval simulations at $z = 7.09$ and $z = 8.04$, respectively. The lower redshifts on the left side of the LC simulations correspond to the later stages of the evolution as compared to the higher redshifts shown on the right side. The ionized regions appear smaller in the LC simulations as compared to their coeval companion at the right side (early stage). Whereas, the ionized regions appear larger in the LC simulations as compared to their coeval case at later stages (left side).

In this work, we assume the plane of the sky is flat. Under the flat-sky approximation, we map the brightness temperature fluctuations $\delta T_b(x, y, z)$ from the Cartesian grid to a 3D rectangular grid in (θ, ν) within our simulation box. We use $\theta_x = x/r$, $\theta_y = y/r$, and $\nu = z/r'$.

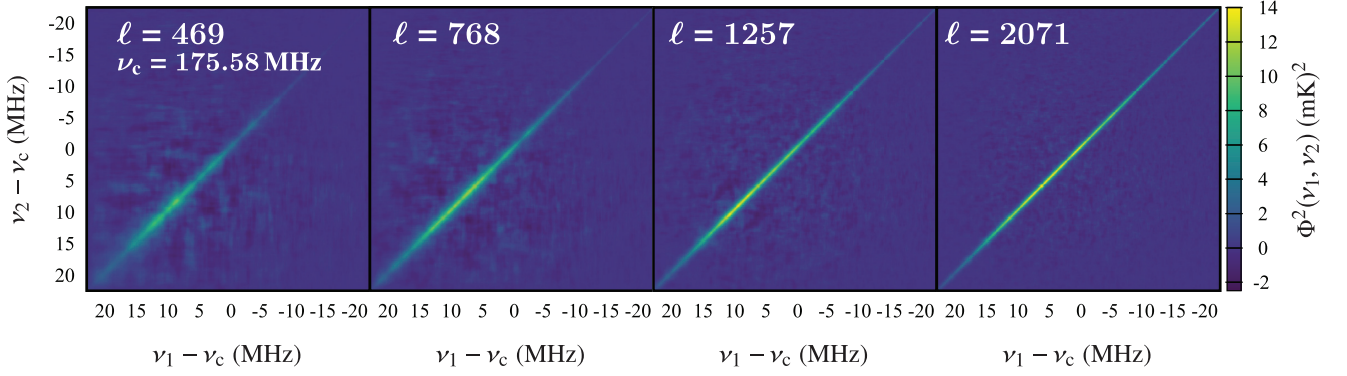


Figure 4. This shows the MAPS $\Phi^2(\nu_1, \nu_2)$ at $\ell = 469, 768, 1257,$ and 2071 (from left to right respectively) for the LC1 at $\nu_c = 175.58$ MHz.

We also keep the angular extent the same at all frequency channels while performing this coordinate transformation.

3 THE MULTIFREQUENCY ANGULAR POWER SPECTRUM

This study concerns the question: ‘How to quantify the statistics of the redshifted EoR HI 21-cm signal $\delta T_b(\hat{n}, \nu)$ when it is non-ergodic along the LoS (i.e. the signal varies significantly along the LoS)?’ (Trott 2016; Mondal et al. 2018, 2019). In the case of the evolving statistical properties of the signal within the observed volume, the 3D Fourier modes \mathbf{k} are not the correct choice of basis. Further, it assumes periodic boundary condition in all directions that is also not justified along the LoS. As a consequence, the power spectrum $P(\mathbf{k})$ is not optimal and gives a biased estimate of the true statistics (Trott 2016; Mondal et al. 2018). To avoid this issue, the previous power spectrum measurements are restricted to individually analysing small redshift intervals (Morales 2005; McQuinn et al. 2006; Zaroubi et al. 2012; Datta et al. 2014; Pober et al. 2014; Ewall-Wice et al. 2016; Shaw et al. 2019).

The above-mentioned properties of the signal necessitate the use of MAPS $C_\ell(\nu_1, \nu_2)$ that quantifies the entire second-order statistics of the EoR 21-cm signal (Mondal et al. 2018). It does not assume the signal to be statistically homogeneous along the LoS. One can decompose $\delta T_b(\hat{n}, \nu)$ into spherical harmonics $Y_\ell^m(\hat{n})$ as

$$\delta T_b(\hat{n}, \nu) = \sum_{\ell, m} a_{\ell m}(\nu) Y_\ell^m(\hat{n}), \quad (4)$$

and define the MAPS using

$$C_\ell(\nu_1, \nu_2) = \langle a_{\ell m}(\nu_1) a_{\ell m}^*(\nu_2) \rangle. \quad (5)$$

The only assumption that goes into this definition is that the EoR 21-cm signal is statistically homogeneous and isotropic in different directions on the sky plane.

In this study, we have chosen to work in the flat-sky approximation, where the redshifted 21-cm brightness temperature fluctuations can be expressed as $\delta T_b(\boldsymbol{\theta}, \nu)$. Here, $\boldsymbol{\theta}$ denotes a 2D vector on the plane of the sky. Instead of $\delta T_b(\boldsymbol{\theta}, \nu)$, we use its 2D Fourier transform $\tilde{T}_{b2}(\mathbf{U}, \nu)$, where \mathbf{U} is the Fourier conjugate of $\boldsymbol{\theta}$ described in the previous section. $\tilde{T}_{b2}(\mathbf{U}, \nu)$ is the primary observable measured in radio interferometric observations. Under the flat-sky approximation, we redefine the MAPS (equation 5) as

$$C_\ell(\nu_1, \nu_2) \equiv C_{2\pi U}(\nu_1, \nu_2) = \Omega^{-1} \langle \tilde{T}_{b2}(\mathbf{U}, \nu_1) \tilde{T}_{b2}(-\mathbf{U}, \nu_2) \rangle, \quad (6)$$

where Ω is the solid angle subtended by the transverse extent of the observation (or simulation) at the location of the observer

and $\ell = 2\pi U$ is the corresponding angular multipole. The above definition of $C_\ell(\nu_1, \nu_2)$ does not assume statistical homogeneity and periodicity along the LoS. However, note that if one imposes statistical homogeneity along the LoS, the MAPS $C_\ell(\nu_1, \nu_2)$ is expected to depend only on the frequency separation $\Delta\nu = |\nu_1 - \nu_2|$, i.e. $C_\ell(\nu_1, \nu_2) \equiv C_\ell(\Delta\nu)$.

The ℓ range of each LC is divided into 10 equally spaced logarithmic bins in our analysis, and each bin is tagged by the bin-averaged value of ℓ i.e. ℓ_i for the i -th bin. Note that the average value ℓ_i varies from LC1 to LC2. In this work, we focus mainly on the intermediate ℓ bins as the detection of the signal will be difficult at large scales ($\ell \lesssim 250$) due to the cosmic variance and at small scales ($\ell \gtrsim 3500$) due to the presence of large system noise. For the LC1, we have shown our results at four different ℓ bins that are $\ell = 469, 768, 1257,$ and 2071 . These ℓ values roughly correspond to comoving scales 119, 72, 44, and 26 Mpc, respectively, at the central frequency $\nu_c = 175.58$ MHz of LC1. For the LC2, we have shown the results at values of $\ell = 486, 796, 1304,$ and 2147 , which roughly correspond to almost the same comoving scales as for the LC1, at the central frequency $\nu_c = 157.08$ MHz. Fig. 4 shows the scaled MAPS $\Phi^2(\nu_1, \nu_2) = [\ell(\ell + 1)C_\ell(\nu_1, \nu_2)]/2\pi$ at four aforementioned values of ℓ for the LC1 simulation, which is centred at a redshift having $\bar{x}_{\text{HI}} \approx 0.50$. Fig. 5 shows the same for the LC2 simulation, which is centred at a redshift with $\bar{x}_{\text{HI}} \approx 0.75$. We see that the MAPS peaks when $\nu_1 = \nu_2$, i.e. along the diagonal line. The diagonal $C_\ell(\nu, \nu)$ evolves considerably with the observed frequency ν . This is a direct consequence of the fact that the signal is non-ergodic along the frequency axis. We also find that the MAPS rapidly falls as the frequency separation $|\nu_1 - \nu_2|$ increases and oscillates around zero for the larger frequency separation. Unlike the 3D power spectrum $P(\mathbf{k})$, which captures only the information regarding the ergodic and periodic part of the signal, the MAPS $C_\ell(\nu_1, \nu_2)$ contains the full information regarding the two-point statistics of the signal (Mondal et al. 2018). One can, in principle, use the entire information contained in $C_\ell(\nu_1, \nu_2)$, i.e. all the diagonal and off-diagonal elements to better constrain the EoR. However, we focus mostly on the diagonal terms $C_\ell(\nu, \nu)$. It will be difficult to detect the off-diagonal C_ℓ s, except for the small frequency separation $|\nu_1 - \nu_2| \sim 1$ MHz, due to poor SNR. We refer the readers to Section 5 for a detailed discussion on the detectability of the MAPS.

Fig. 6 shows the diagonal components of the scaled MAPS $\Phi^2(\nu, \nu)$ as a function of ν for ℓ values considered above for both simulations LC1 (black) and LC2 (red). It also shows the ergodic part of the signal $\Phi^2(\nu_c, \nu_c)$ that is calculated at the central frequency ν_c , which is different for the LC1 and LC2 simulation.

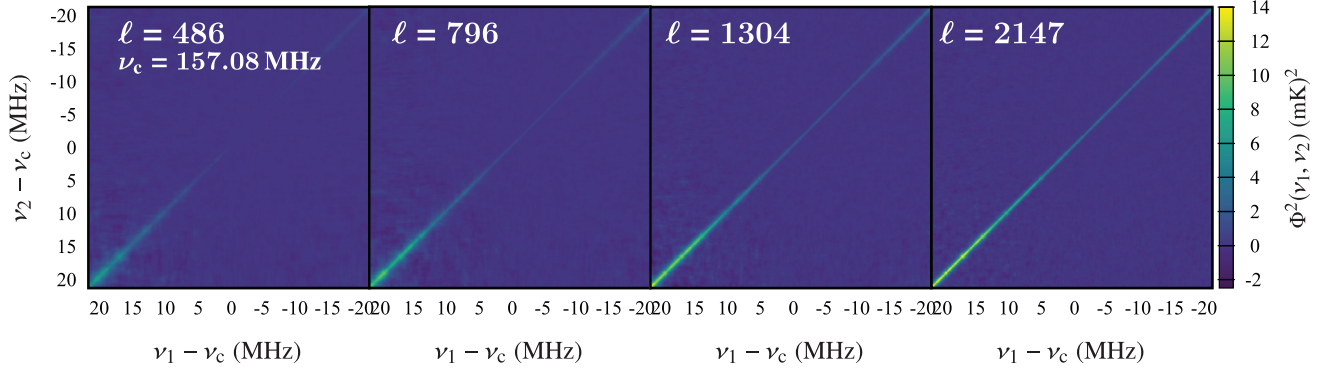


Figure 5. Same as Fig. 4 at $\ell = 486, 796, 1304,$ and 2147 (from left to right respectively) for the LC2 at $\nu_c = 157.08$ MHz.

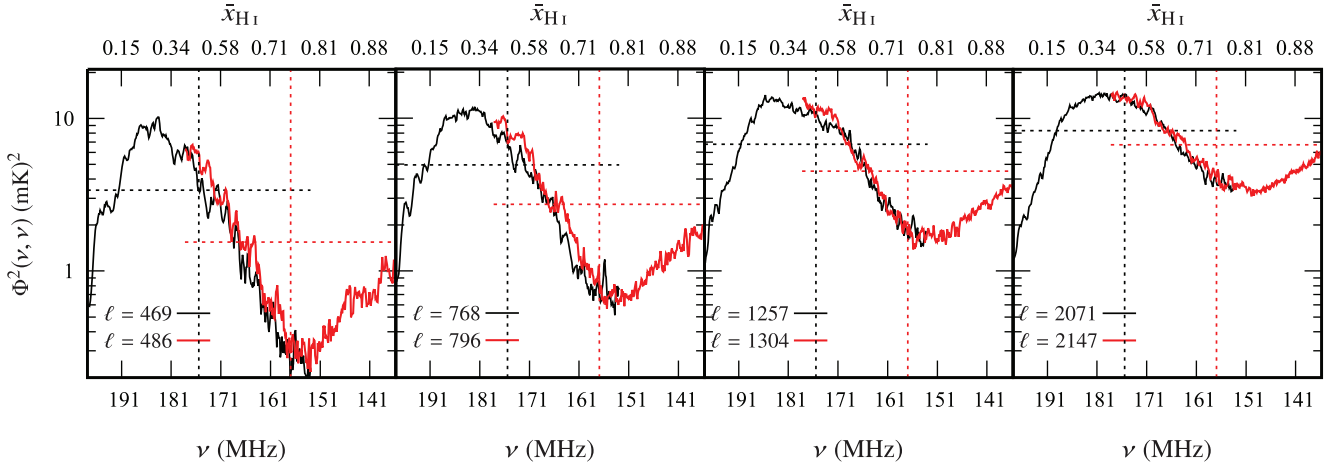


Figure 6. This shows the diagonal components of the scale-independent MAPS $\Phi^2(\nu, \nu)$ for LC1 (black) and LC2 (red). The LC1 and LC2 are, respectively, centred at frequency 175.58 and 157.08 MHz (vertical dashed lines). We also show the ergodic component (mean) of MAPS $[\ell(\ell + 1)C_\ell^E(\nu, \nu)/2\pi]$ (horizontal dashed lines). The $\bar{x}_{H\text{I}}$ values corresponding to the frequencies are shown in the top x-axis.

The 3D power spectrum $P(k)$ misses the part that is deviated from these horizontal dashed lines. We further see in Fig. 6 that $\Phi^2(\nu, \nu)$ peaks around a frequency corresponding to the global neutral fraction $\bar{x}_{H\text{I}} \approx 0.35$ for both simulations. This is due to the presence of a significant number of large ionized bubbles at that stage of the EoR. The power spectrum at higher frequency decreases due to the rapid decline of the neutral fraction $\bar{x}_{H\text{I}}$. The characteristic size of ionized bubbles decreases at lower frequencies, which causes the power spectrum to decrease. Similar results have been found in earlier studies (McQuinn et al. 2007; Lidz et al. 2008; Choudhury, Haehnelt & Regan 2009; Mesinger, Furlanetto & Cen 2011). We also notice that there is a ‘dip’ in the power spectrum $\Phi^2(\nu, \nu)$ around a frequency corresponding to the global neutral fraction $\bar{x}_{H\text{I}} \approx 0.8$ for all ℓ modes for both simulations. During the early stages of reionization, the high-density regions get ionized first, and as a consequence, the large-scale power decreases. This is reflected by the drop in the power across the four ℓ panels when the neutral fraction is large. Later, as the reionization progresses further, the creation and growth of the ionized regions increase the power spectrum which peaks around $\bar{x}_{H\text{I}} \approx 0.35$. Datta et al. (2014) have investigated the impact of the LC effect considering a similar reionization model and find a similar dip around $\bar{x}_{H\text{I}} \sim 0.8$. The frequencies at which the minimum and maximum occur may

change for different ℓ values. However, we do not see any significant change in the locations of the maxima and minima for the ℓ modes we consider.

Fig. 7 shows the angular power spectrum of the EoR 21-cm brightness temperature fluctuations as a function of ℓ at four different frequency $\nu = 185$ (LC1), 170 (LC1), 155 (LC2), and 140 MHz (LC2). Note that the angular power spectrum shown in this plot is a special case of MAPS where $\nu_1 = \nu_2$. The basic assumption of our model is that the hydrogen traces the underlying dark matter distribution. As a result of this, the shape of the 21-cm angular power spectra is roughly the same as the dark matter angular power spectrum at the start of reionization ($\nu \gtrsim 140$ MHz). As discussed above (Fig. 6), during the early stages of reionization, the high-density regions get ionized first in the inside-out scenario, and as a consequence, the power spectrum drops at $\nu = 155$ MHz. As reionization progresses, the creation and growth of the ionized bubbles increase the power at $\nu = 170$ MHz. The contrast of the brightness temperature fluctuation field peaks on large scales at $\nu \approx 185$ MHz which corresponds to $\bar{x}_{H\text{I}} \approx 0.35$ in our fiducial reionization model. This further raises the power of signal at small ℓ (large length-scales). However, growth of the ionized regions reduces contrast of the signal at small length-scales showing drop in power at the corresponding ℓ values.

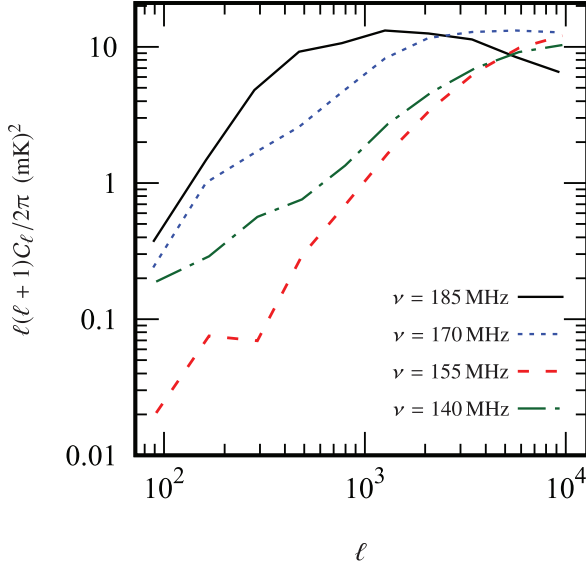


Figure 7. This shows the angular power spectrum of the EoR 21-cm brightness temperature fluctuations as a function of ℓ at four different frequency $\nu = 185$ (LC1), 170 (LC1), 155 (LC2), and 140 MHz (LC2) for a particular case of MAPS where $\nu_1 = \nu_2$.

4 OBSERVATIONAL CONSIDERATIONS

We now consider observations with a radio interferometric array where the fundamental quantity is the visibility that is measured by each pair of antennas in the array. Considering any particular pair with \mathbf{d}_n being the antenna separation projected on the plane perpendicular to the LoS, the visibility measured at frequency ν_i and baseline $\mathbf{U}_n = \mathbf{d}_n/\lambda_i$ provides a direct estimate of $\tilde{T}_{b2}(\mathbf{U}_n, \nu_i)$ at the Fourier mode \mathbf{U}_n . Taking into account $\tilde{T}_{b2}^N(\mathbf{U}, \nu)$, the system noise contribution that is inherent in any radio interferometric observation, the measured visibility actually provides us with $\tilde{T}_{b2}^t(\mathbf{U}_n, \nu_i) = \tilde{T}_{b2}(\mathbf{U}_n, \nu_i) + \tilde{T}_{b2}^N(\mathbf{U}_n, \nu_i)$, where we have assumed that the foregrounds have been completely removed and there are no calibration errors. The system noise at different baselines and frequency channels is uncorrelated. Using this in equation (6) for the MAPS, we obtain

$$C_\ell^t(\nu_1, \nu_2) = C_\ell(\nu_1, \nu_2) + \delta_{\nu_1\nu_2}^K C_\ell^N(\nu_1, \nu_2), \quad (7)$$

which can be estimated from the observed visibilities. Following the prescription in Bharadwaj et al. (2018), it is possible to avoid noise bias $C_\ell^N(\nu_1, \nu_2)$ and obtain an unbiased estimate of $C_\ell(\nu_1, \nu_2)$ from the measured visibilities. However, the noise contributions still persist in the error estimates and this cannot be avoided. In this work, we compute the error variance to predict the SNR of measuring MAPS using the upcoming SKA-Low. This also involves the estimation of system noise for which we use the telescope specifications of SKA-Low taken from the current proposed configuration document (see footnote 7). Some important specifications⁸ that have been used in the computation of $C_\ell^N(\nu, \nu)$ are tabulated in Table 1.

We consider observations tracking a field at declination Dec. = -30° for 8 h per night with 60 s integration time following the formalism adopted by Shaw et al. (2019). We restrict our analysis to the baselines \mathbf{U} corresponding to the antenna separations $|\mathbf{d}| <$

⁸The specifications assumed here may change in the final implementation of the telescope.

Table 1. This tabulates the telescope specifications for the current proposed configuration of SKA-Low.

Parameters	Values
Number of stations	512
Diameter of each station (D)	35 m
Operation frequency range	50–350 MHz
Receiver temperature (T_{rec})	100 K
Maximum baseline separation	~ 19 km

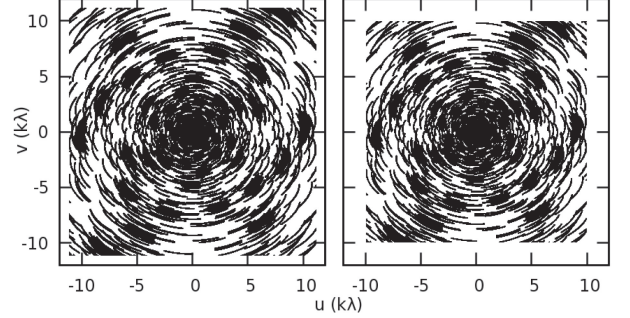


Figure 8. The SKA-Low uv coverage with phase centre at RA = $13^{\text{h}} 2^{\text{m}} 31.5^{\text{s}}$ and Dec. = $-26^\circ 49' 29''$ for a total observation time of 2 h. u and v are projected antenna separation (for $|\mathbf{d}| < 19$ km) in the unit of $k\lambda$ at the central frequencies $\nu_c = 175.58$ MHz (left) and $\nu_c = 157.08$ MHz (right).

19 km, as the baseline distribution falls off rapidly at larger $|\mathbf{d}|$ values. Fig. 8 shows the simulated SKA-Low baseline \mathbf{U} distribution (uv coverage) at the two different central frequencies, corresponding to LC1 and LC2, respectively. The signals at two different baselines \mathbf{U} separated by $< D/\lambda_i$ are correlated due to the overlap of the antenna beam pattern (Bharadwaj & Pandey 2003; Bharadwaj & Ali 2005). We grid the baselines \mathbf{U}_m with a grid of size $\Delta U_x = \Delta U_y = D/\lambda_i$ and count the number of measurements $\tau(\mathbf{U}_g)$ that lie within a pixel centred at any grid point \mathbf{U}_g .

We estimate the noise MAPS at the grid point \mathbf{U}_g following the calculation presented in White et al. (1999), Zaldarriaga, Furlanetto & Hernquist (2004), and Shaw et al. (2019) as

$$C_{\ell_g}^N(\nu, \nu) = \frac{T_{\text{sys}}^2 \lambda^4}{N_p N_t \Delta t \Delta \nu a^2 \tau(\mathbf{U}_g)} \times \frac{1}{\int d\mathbf{U}' |\tilde{A}(\mathbf{U} - \mathbf{U}')|^2} \\ = \frac{8 \text{ hrs}}{t_{\text{obs}}} \times \frac{C^0(\nu)}{\tau(\mathbf{U}_g)}. \quad (8)$$

Here, the system temperature T_{sys} is a sum of the sky temperature $T_{\text{sky}} = 60\lambda^{2.55}$ K (Fixsen et al. 2011) and the receiver temperature T_{rec} . N_p is the number of polarizations, N_t is the number of observed nights, Δt is the integration time, a is the area of individual antenna in the array, and $\tilde{A}(\mathbf{U})$ is the Fourier transform of the primary beam of a station $A(\theta)$, which is approximated with a Gaussian $e^{-(\theta/\theta_0)^2}$ (Choudhuri et al. 2014; Shaw et al. 2019). We express the total observation time using $t_{\text{obs}} = 8 \text{ h} \times N_t$, and this notation is used in the rest of the paper.

4.1 The binned weighted MAPS estimator

The simulated observations under consideration have $\sim 300 \times 300$ grid points on the \mathbf{U} plane and 313 frequency channels. This comes out to ~ 14 million independent measurements of the MAPS that

is computationally very expensive to deal with. Another problem is that the measurements at every individual grid point \mathbf{U}_g will be very noisy. To tackle these issues, we bin the U space. We, however, lose the information at individual \mathbf{U}_g modes. This not only solves the computation problem but also increases the SNR of measurement within a bin. We use the binned weighted MAPS estimator $\hat{\mathcal{C}}_{\ell_i}^t(\nu_1, \nu_2)$, which is the sum of the weighted brightness temperature fluctuation correlations between various grids within the bin. Exploiting the symmetry $\hat{\mathcal{C}}_{\ell_i}^t(\nu_1, \nu_2) = \hat{\mathcal{C}}_{\ell_i}^t(\nu_2, \nu_1)$, the estimator $\hat{\mathcal{C}}_{\ell_i}^t(\nu_1, \nu_2)$ for the i -th bin is written as

$$\begin{aligned} \hat{\mathcal{C}}_{\ell_i}^t(\nu_1, \nu_2) &= \frac{1}{2\Omega} \sum_{\mathbf{U}_{g_i}} \hat{w}(\mathbf{U}_{g_i}, \nu_1) \hat{w}(\mathbf{U}_{g_i}, \nu_2) \\ &\times [\tilde{T}_{b2}^t(\mathbf{U}_{g_i}, \nu_1) \tilde{T}_{b2}^t(-\mathbf{U}_{g_i}, \nu_2) \\ &+ \tilde{T}_{b2}^t(\mathbf{U}_{g_i}, \nu_2) \tilde{T}_{b2}^t(-\mathbf{U}_{g_i}, \nu_1)], \end{aligned} \quad (9)$$

where the sum $\sum_{\mathbf{U}_{g_i}}$ is over the \mathbf{U}_g grids within the i -th bin and $\hat{w}(\mathbf{U}_g, \nu)$ is the weight associated with the grid \mathbf{U}_g at frequency ν . Here, the angular multipole $\ell_i = 2\pi U_i$ (or U_i) is the weighted average of all \mathbf{U}_g in the i -th bin. We have used equally spaced logarithmic binning, and the bins here are semi-annuli of the width $\Delta U_i \propto U_i$ (restricted to one half of the U plane as the signal is real, i.e. $\tilde{T}_{b2}^{t*}(\mathbf{U}_{g_i}, \nu_1) = \tilde{T}_{b2}^t(-\mathbf{U}_{g_i}, \nu_1)$).

The ensemble average of the estimator gives the bin-averaged MAPS

$$\begin{aligned} \langle \hat{\mathcal{C}}_{\ell_i}^t(\nu_1, \nu_2) \rangle &\equiv \bar{\mathcal{C}}_{\ell_i}^t(\nu_1, \nu_2) \\ &= \bar{\mathcal{C}}_{\ell_i}(\nu_1, \nu_2) + \delta_{\nu_1 \nu_2}^K \bar{\mathcal{C}}_{\ell_i}^N(\nu_1, \nu_2). \end{aligned} \quad (10)$$

As mentioned earlier, it is possible to avoid the noise bias $\bar{\mathcal{C}}_{\ell_i}^N(\nu, \nu)$ (Bharadwaj et al. 2018) by subtracting out the contribution of the self-correlation of visibility from itself. This also leads to a loss of a part of the signal. However, this loss is extremely small (< 0.01 per cent) for long observations ($t_{\text{obs}} \sim 100$ h or larger) with 16 s integration time. It is therefore quite well justified to assume that we can obtain an unbiased estimate of $\bar{\mathcal{C}}_{\ell_i}(\nu_1, \nu_2)$. In the subsequent analysis, we also do not consider any change in the weights along the frequency direction and express equation 9 as

$$\begin{aligned} \hat{\mathcal{C}}_{\ell_i}^t(\nu_1, \nu_2) &= \frac{1}{2\Omega} \sum_{\mathbf{U}_{g_i}} w(\mathbf{U}_{g_i}) [\tilde{T}_{b2}^t(\mathbf{U}_{g_i}, \nu_1) \tilde{T}_{b2}^t(-\mathbf{U}_{g_i}, \nu_2) \\ &+ \tilde{T}_{b2}^t(\mathbf{U}_{g_i}, \nu_2) \tilde{T}_{b2}^t(-\mathbf{U}_{g_i}, \nu_1)]. \end{aligned} \quad (11)$$

The weights $w(\mathbf{U}_{g_i})$ are normalized such that $\sum_{\mathbf{U}_{g_i}} w_{g_i} = 1$ where the sum runs over each grid point within a particular U bin. As discussed later, the weights are selected in order to maximize the SNR of $\bar{\mathcal{C}}_{\ell_i}(\nu_1, \nu_2)$ for each bin. This takes into account that the baselines \mathbf{U}_m do not uniformly sample the different grid points \mathbf{U}_g , and consequently the ratio $\mathcal{C}_{\ell_{g_i}}(\nu_1, \nu_2)/\mathcal{C}_{\ell_{g_i}}^N(\nu_1, \nu_2)$ varies across the different grid points within a bin.

4.2 The error estimates

The EoR 21-cm signal is a highly non-Gaussian field (see e.g. Bharadwaj & Pandey 2005; Mondal et al. 2015; Yoshiura et al. 2015; Majumdar et al. 2018). The non-Gaussian effects will play a significant role in the error estimates for the EoR 21-cm MAPS. The Gaussian components in observed visibilities $\tilde{T}_{b2}(\mathbf{U}, \nu)$ are independent at different baselines. It is the non-Gaussian components that are correlated and give rise to non-zero higher order

statistics such as bispectrum, trispectrum etc. The cosmic variance of the MAPS will get additional contributions from the non-zero trispectra (see equation 2 of Mondal, Bharadwaj & Majumdar 2017) that is essentially the Fourier conjugate of the four-point correlation function (see e.g. equation 2 of Adhikari & Huterer 2019). The angular trispectra will also introduce correlations between the errors in MAPS at different ℓ modes. Mondal, Bharadwaj & Majumdar (2016) and Mondal et al. (2017) have quantitatively demonstrated the impact of non-Gaussianity in the context of estimating the EoR 21-cm 3D power spectrum cosmic variance. Recently, Shaw et al. (2019) have shown that, in presence of the Gaussian system noise and foreground contamination, the contribution of trispectrum to the error variance is significant within a limited range of k modes, and mostly during the later stages of reionization ($z \lesssim 10$). Considering the SKA-Low observations, we can ignore the contribution of the non-Gaussianity of the signal in the observed MAPS error covariance. Furthermore, estimating the angular trispectrum of the LC signal is computationally challenging. Hence for simplicity, we do not consider the non-Gaussian nature of the EoR 21-cm signal in our calculations and assume the error estimate of the MAPS is completely determined by that of the Gaussian random field predictions. Following the calculation presented in Appendix A, we write the MAPS error covariance as

$$\begin{aligned} \mathbf{X}_{12,34}^{\ell_i} &= \langle [\delta \mathcal{C}_{\ell_i}^t(\nu_1, \nu_2)] [\delta \mathcal{C}_{\ell_i}^t(\nu_3, \nu_4)] \rangle \\ &= \frac{1}{2} \sum_{\mathbf{U}_{g_i}} w_{g_i}^2 [\mathcal{C}_{\ell_{g_i}}^t(\nu_1, \nu_3) \mathcal{C}_{\ell_{g_i}}^t(\nu_2, \nu_4) \\ &+ \mathcal{C}_{\ell_{g_i}}^t(\nu_1, \nu_4) \mathcal{C}_{\ell_{g_i}}^t(\nu_2, \nu_3)], \end{aligned} \quad (12)$$

where the sum is over all the \mathbf{U}_{g_i} grids within the i -th bin and $w_{g_i} \equiv w(\mathbf{U}_{g_i})$. The variance in the measured $\bar{\mathcal{C}}_{\ell_i}^t(\nu_1, \nu_2)$ is thus given by

$$\begin{aligned} \mathbf{X}_{12,12}^{\ell_i} &= [\sigma_{12}^{\ell_i}]^2 = \langle [\delta \mathcal{C}_{\ell_i}^t(\nu_1, \nu_2)]^2 \rangle \\ &= \frac{1}{2} \sum_{\mathbf{U}_{g_i}} w_{g_i}^2 [\mathcal{C}_{\ell_{g_i}}^t(\nu_1, \nu_1) \mathcal{C}_{\ell_{g_i}}^t(\nu_2, \nu_2) + \{\mathcal{C}_{\ell_{g_i}}^t(\nu_1, \nu_2)\}^2] \\ &= \frac{1}{2} \sum_{\mathbf{U}_{g_i}} w_{g_i}^2 [\{\mathcal{C}_{\ell_{g_i}}(\nu_1, \nu_1) + \mathcal{C}_{\ell_{g_i}}^N(\nu_1, \nu_1)\} \\ &\times \{\mathcal{C}_{\ell_{g_i}}(\nu_2, \nu_2) + \mathcal{C}_{\ell_{g_i}}^N(\nu_2, \nu_2)\} \\ &+ \{\mathcal{C}_{\ell_{g_i}}(\nu_1, \nu_2) + \delta_{\nu_1 \nu_2}^K \mathcal{C}_{\ell_{g_i}}^N(\nu_1, \nu_2)\}^2], \end{aligned} \quad (13)$$

where the sum is over the grids points \mathbf{U}_{g_i} within the i -th bin. We know that the MAPS signal peaks along the diagonal elements $\nu_1 = \nu_2$, where the error variance (using equation 13) is given by

$$[\sigma_{11}^{\ell_i}]^2 = \sum_{\mathbf{U}_{g_i}} w_{g_i}^2 [\mathcal{C}_{\ell_{g_i}}(\nu_1, \nu_1) + \mathcal{C}_{\ell_{g_i}}^N(\nu_1, \nu_1)]^2. \quad (14)$$

The two terms in the right-hand side of equation 14 are due to the cosmic variance and the system noise, respectively. We require the EoR 21-cm MAPS $\mathcal{C}_{\ell_g}(\nu_1, \nu_2)$, the noise MAPS $\mathcal{C}_{\ell_g}^N(\nu, \nu)$ and appropriate weights w_g to estimate the errors (equations 13 and 14).

We obtain the weights by extremizing the SNR with respect to w_g with an assumption that the EoR 21-cm MAPS does not vary much within an ℓ -bin and therefore $\mathcal{C}_{\ell_{g_i}}(\nu_1, \nu_2) = \bar{\mathcal{C}}_{\ell_i}(\nu_1, \nu_2)$. Note that we consider the variation of the noise $\mathcal{C}_{\ell_{g_i}}^N(\nu, \nu)$ across the grid points within a bin. Considering two different frequency channels at ν_1 and ν_2 , for a particular ℓ -bin, we can then express the unnormalized

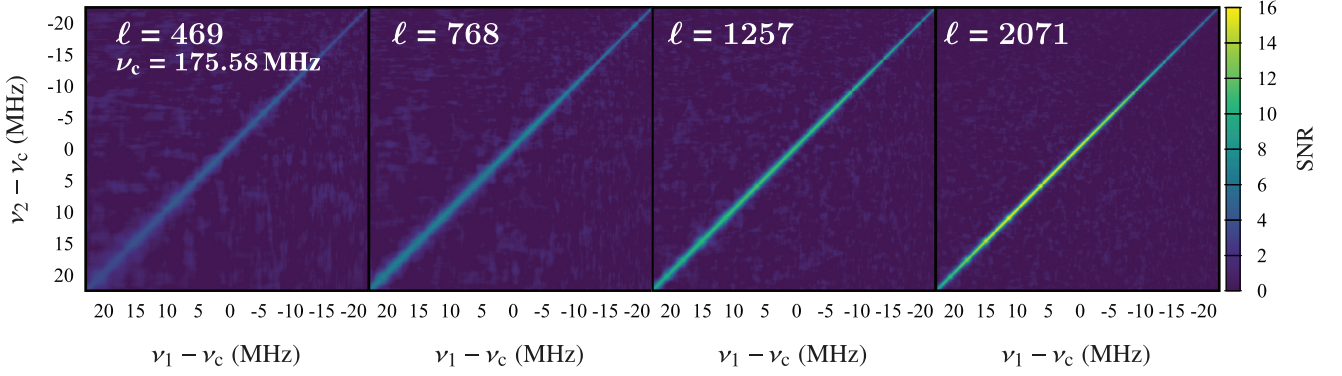


Figure 9. This shows the SNR for MAPS at $\ell = 469, 768, 1257,$ and 2071 (from left to right, respectively) for $t_{\text{obs}} = 1024$ h for the LC1.

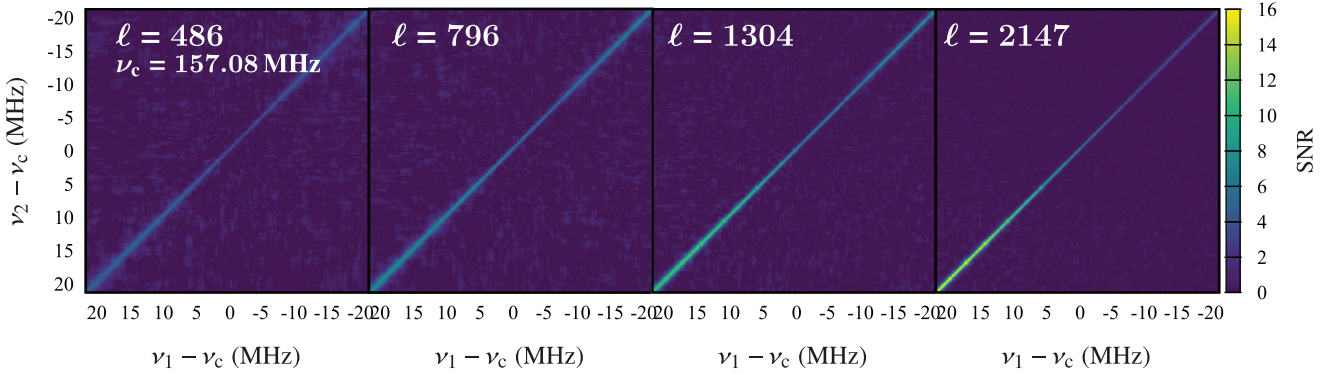


Figure 10. Same as Fig. 9 at $\ell = 486, 796, 1304,$ and 2147 (from left to right, respectively) for $t_{\text{obs}} = 1024$ h for the LC2.

weights in equation 13 as

$$\begin{aligned} \tilde{w}_g = & \left[\{ \mathcal{C}_{\ell_{\text{gi}}}(\nu_1, \nu_1) + \mathcal{C}_{\ell_{\text{gi}}}^{\text{N}}(\nu_1, \nu_1) \} \{ \mathcal{C}_{\ell_{\text{gi}}}(\nu_2, \nu_2) + \mathcal{C}_{\ell_{\text{gi}}}^{\text{N}}(\nu_2, \nu_2) \} \right. \\ & \left. + \{ \bar{\mathcal{C}}_{\ell_g}(\nu_1, \nu_2) + \delta_{\nu_1 \nu_2}^{\text{K}} \mathcal{C}_{\ell_g}^{\text{N}}(\nu_1, \nu_2) \}^2 \right]^{-1}. \end{aligned} \quad (15)$$

This implies that the grid points with higher noise have lower weights and contribute less to the estimator. The grid points that are unsampled during the observation (i.e. $\tau(\mathbf{U}_g) = 0$ and $\mathcal{C}_{\ell_g}^{\text{N}}(\nu, \nu) = \infty$) have zero weights, hence they do not contribute. Using equations (13) and (15), we have the expression for the error variance

$$[\sigma_{12}^{\ell_i}]^2 = \frac{1}{2} \times \frac{1}{\sum_{U_{\text{gi}}} \tilde{w}_{\text{gi}}}. \quad (16)$$

We now discuss the behaviour of the error variance $[\sigma_{12}^{\ell_i}]^2$ (equation 16) in two different scenarios. The MAPS error variance consists of the cosmic variance and the system noise $\mathcal{C}_{\ell_g}^{\text{N}}(\nu, \nu)$. We see from equation 8 that the noise contribution drops off as $\mathcal{C}_{\ell_g}^{\text{N}}(\nu, \nu) \propto 1/t_{\text{obs}}$ with an increase in observation time. For small observation times, the estimated error variance is thus dominated by the large system noise, and from equation 16, we have

$$[\sigma_{12}^{\ell_i}]^2 \simeq \frac{\mathcal{C}^0(\nu_1)\mathcal{C}^0(\nu_2) + \delta_{\nu_1 \nu_2}^{\text{K}} [\mathcal{C}^0(\nu_1, \nu_2)]^2}{2 \times \sum_{U_{\text{gi}}} [\tau(\mathbf{U}_{\text{gi}})]^2} \times \left(\frac{8h}{t_{\text{obs}}} \right)^2. \quad (17)$$

In contrast, we have the other extreme $\mathcal{C}_{\ell_g}^{\text{N}}(\nu, \nu) \simeq 0$ for very large observation times ($t_{\text{obs}} \rightarrow \infty$). In this case, the error variance

approaches the cosmic variance (CV) limit and we have

$$[\sigma_{12}^{\ell_i}]^2 \simeq \frac{\bar{\mathcal{C}}_{\ell_{\text{gi}}}(\nu_1, \nu_1)\bar{\mathcal{C}}_{\ell_{\text{gi}}}(\nu_2, \nu_2) + [\bar{\mathcal{C}}_{\ell_{\text{gi}}}(\nu_1, \nu_2)]^2}{2N_{\text{gi}}}, \quad (18)$$

where N_{gi} is the number of sampled grid points in the i -th bin.

5 RESULTS

Figs 9 and 10 show the SNR for measuring the MAPS at the four representative ℓ values considered here for LC1 and LC2, respectively. For the moderate observation time $t_{\text{obs}} = 1024$ h, we see a correspondence of behaviour between the SNR for MAPS and the signal (Figs 4 and 5). They both peak along the diagonal and fall rapidly away from the diagonal. The previous error estimates (Morales 2005; McQuinn et al. 2006; Zaroubi et al. 2012; Datta et al. 2014; Pober et al. 2014; Ewall-Wice et al. 2016; Shaw et al. 2019) are restricted to individually analysing small frequency intervals centred at a particular frequency. However, we see that the error estimates, as well as the SNR values for MAPS, change with the frequency across the bandwidth. We shall discuss this in more detail in the following paragraph.

In the subsequent results, we focus on the diagonal elements $\nu_1 = \nu_2$ of MAPS. Figs 11 and 12 show $\Phi^2(\nu, \nu)$ and the corresponding 5σ rms error estimates for LC1 and LC2, respectively. In these figures, the bottom panels show the relative difference $\Delta\Phi^2/\Phi^2 = (\Phi^2(\nu, \nu) - 5\sigma_{11})/\Phi^2(\nu, \nu)$. The positive values in the bottom panels correspond to values that are above the 5σ noise level. In the following analysis, we have considered four different observation

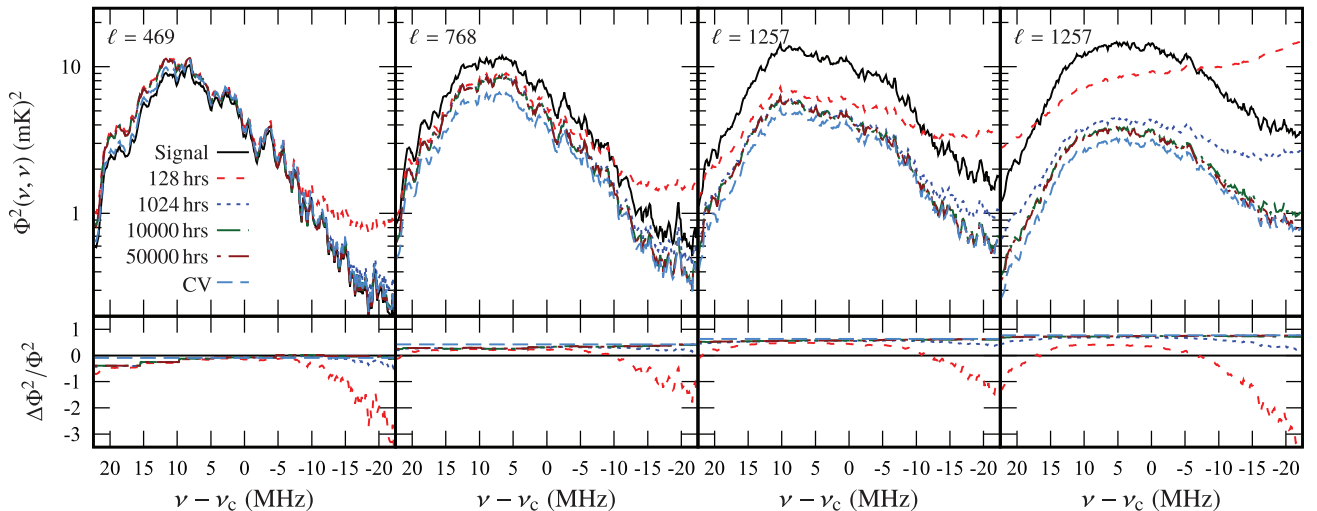


Figure 11. This shows the diagonal components of the scale-independent MAPS $\Phi^2(\nu, \nu)$ and the corresponding 5σ rms error estimates for the LC1. We consider four different observation times t_{obs} . We also show CV that corresponds to $t_{\text{obs}} \rightarrow \infty$. The bottom panels show the relative difference $\Delta\Phi^2/\Phi^2 = (\Phi^2(\nu, \nu) - 5\sigma_{11})/\Phi^2(\nu, \nu)$. The positive values in the bottom panels correspond to values that are above the 5σ noise level.

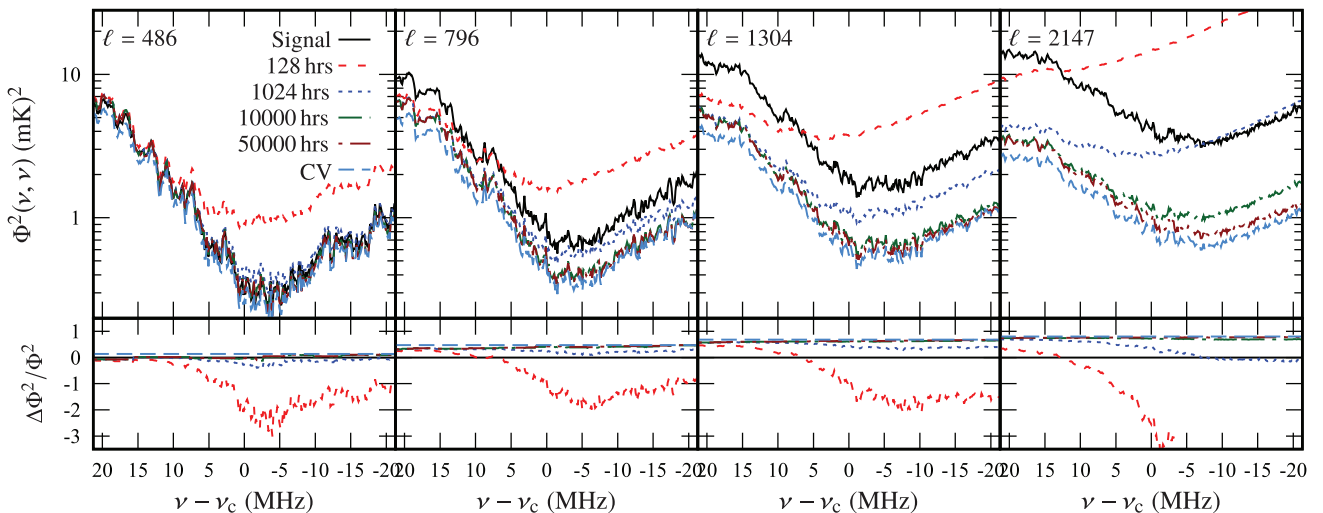


Figure 12. Same as Fig. 11 for the LC2.

times $t_{\text{obs}} = 128, 1024, 10000,$ and 50000 h. We also show CV, which corresponds to $t_{\text{obs}} \rightarrow \infty$ and the system noise approaches zero. As discussed above, the cosmic variance and the system noise contribute to the total error budget (equation 14). Considering the behaviour of rms error at large angular scales, we see that rms error is not much affected even if t_{obs} is increased. Whereas the rms error decreases as t_{obs} is increased at small angular scales. This confirms the fact that the cosmic variance dominates the total error at small ℓ and the system noise contribution dominates at large ℓ . We also see that the rms error increases with decreasing frequency across the bandwidth of our simulations. This is due to the fact that the system noise contribution increases (equation 8) with decreasing frequency. Considering Fig. 11, we see that for any feasible t_{obs} a 5σ detection will not be possible at $\ell \leq 496$. The condition improves at $\ell = 796$, where SKA will be able to measure the MAPS at $\geq 5\sigma$ confidence over ~ 25 MHz frequency band for $t_{\text{obs}} \geq 128$ h. $\ell = 1257$ is a better scenario among the four ℓ values, where 5σ detection will be possible roughly across the entire observational bandwidth for $t_{\text{obs}} \geq 128$ h. Whereas, the frequency band allowed for $\geq 5\sigma$

detection reduces at $\ell = 2071$ due to system noise domination. We find the behaviour in Fig. 12 is similar to that in LC1. The optimal angular multipole for detection, among the four ℓ values, is $\ell = 1304$ in Fig. 12. The difference here is that the MAPS signal peaks at one end of the band as compared to LC1, where the signal peaks around the centre of the frequency band.

Fig. 13 plots the SNR for the diagonal elements of MAPS as a function of ℓ and frequency for four observation times $t_{\text{obs}} = 128, 1024, 10000,$ and 50000 h (from left to right, respectively) for LC1 simulation. It also shows various contours corresponding to different SNR values. We see that the SNR peaks at intermediate scales corresponding to ℓ of a few thousand. This is because the cosmic variance dominates the total error at large scales whereas the system noise dominates at small scales. Since the cosmic variance part is independent of the total observing time, the SNR at large scales does not improve by increasing the total observing time. However, the SNR at small scales (large ℓ) increases with the total observing time. Consequently, the scale at which the SNR peaks moves towards the higher ℓ values. The SNR drops at lower

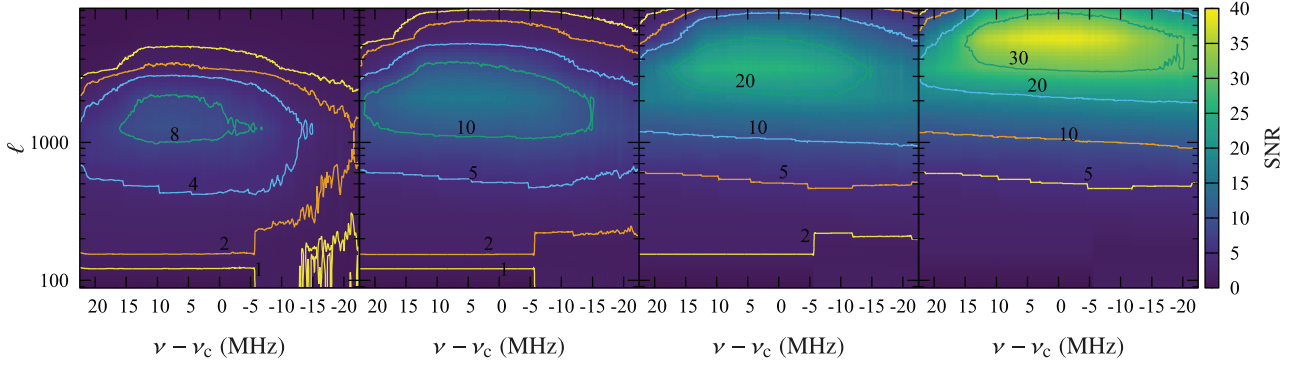


Figure 13. This shows the SNR of the diagonal components of MAPS $\Phi^2(\nu, \nu)$ as a function ℓ at $t_{\text{obs}} = 128, 1024, 10000,$ and 50000 h (from left to right respectively) for the LC1.

frequencies (higher redshifts) because of the rise in the system temperature. We find similar behaviour in Fig. 14 which shows results for LC2 simulation. The only difference is that the SNR is maximum at the highest frequency (lowest redshift) explored here. This is because the power spectrum in this simulation is maximum at the highest frequency unlike the LC1 simulation where the power spectrum peaks at some intermediate frequency.

6 EFFECTS OF FOREGROUNDS

Foregrounds pose a major challenge even for the statistical detection of the EoR 21-cm signal. Two main approaches have been proposed in the literature to tackle the foreground problem. One of them is the *foreground removal* (Morales, Bowman & Hewitt 2006; Ali et al. 2008; Harker et al. 2009; Bonaldi & Brown 2015; Pober et al. 2016; Mertens, Ghosh & Koopmans 2018; Mertens et al. 2020), in which the foreground is modelled and removed from the observed 21-cm signal. The forecast of this analysis till now has assumed that the foregrounds have been completely removed, and we refer this as the ‘Optimistic’ scenario (Chatterjee & Bharadwaj 2018; Shaw et al. 2019).

The other technique is termed as *foreground avoidance*. The foreground contamination is found to be restricted within a wedge shaped region in the $(k_{\perp}, k_{\parallel})$ plane (Datta, Bowman & Carilli 2010) with the wedge boundary defined by

$$k_{\parallel} = \left[\frac{r_c \sin(\theta_L)}{r'_c v_c} \right] k_{\perp}, \quad (19)$$

where r_c is the comoving distance corresponding to the central frequency ν_c , $r'_c = \frac{\partial r_c}{\partial \nu} |_{\nu_c}$ and θ_L is the angle on the sky with respect to the zenith from which the foregrounds contaminate the EoR 21-cm signal. The value of θ_L and hence the slope of the wedge is determined by the level of foreground contamination (Morales et al. 2012; Hassan, Andrianomena & Doughty 2019). The region outside the foreground wedge, the ‘EoR Window’, is utilized for estimating the EoR 21-cm 3D power spectrum $P(\mathbf{k})$ (Pober et al. 2013; Kerrigan et al. 2018). The upper limit of the wedge boundary is set by the horizon for which $\theta_L = 90^\circ$. We refer to this case as the ‘Pessimistic’ scenario (Chatterjee & Bharadwaj 2018; Shaw et al. 2019).

Ghosh et al. (2011) and Choudhuri et al. (2016) have shown that tapering the sky response in telescope’s field of view restricts the θ_L to an angle smaller than the horizon limit. In this analysis, we consider two different tapering situations which assume $\theta_L = 3 \times (\text{FWHM}/2)$ and $\theta_L = 9 \times (\text{FWHM}/2)$. Here, FWHM is the full

width at half-maximum of the SKA-Low primary beam. We refer these two tapered cases as the ‘Mild’ and ‘Moderate’ scenarios, respectively (Chatterjee & Bharadwaj 2018; Shaw et al. 2019).

As mentioned earlier, our estimator $\mathcal{C}_{\ell}(\nu_1, \nu_2)$ does not assume that the signal is ergodic and periodic along the LoS direction. Therefore, it is not straightforward to consider the foreground wedge in our analysis as this explicitly assumes the signal to be ergodic and periodic along LoS direction. Following Mondal et al. (2018), we define $\mathcal{C}_{\ell}^{\text{EP}}(\nu_1, \nu_2)$ which is the ergodic (E) and periodic (P) component of $\mathcal{C}_{\ell}(\nu_1, \nu_2)$. The $\mathcal{C}_{\ell}^{\text{EP}}(\nu_1, \nu_2)$ is estimated from the measured $\mathcal{C}_{\ell}(\nu_1, \nu_2)$ by imposing the conditions $\mathcal{C}_{\ell}^{\text{EP}}(\nu_1, \nu_2) = \mathcal{C}_{\ell}^{\text{EP}}(|\nu_1 - \nu_2|) = \mathcal{C}_{\ell}^{\text{EP}}(\Delta\nu)$ (ergodicity) and $\mathcal{C}_{\ell}^{\text{EP}}(\Delta\nu) = \mathcal{C}_{\ell}^{\text{EP}}(B - \Delta\nu)$ (periodicity). Under these assumptions, we can estimate $\mathcal{C}_{\ell}^{\text{EP}}(\Delta\nu)$ using equation (21) of Datta et al. (2007) as

$$\mathcal{C}_{\ell}^{\text{EP}}(\Delta\nu) = \frac{1}{\pi r_c^2} \int_0^{\infty} dk_{\parallel} \cos(k_{\parallel} r'_c \Delta\nu) P(k_{\perp}, k_{\parallel}). \quad (20)$$

We compute the foreground ‘wedge’ boundary in $(k_{\perp}, k_{\parallel})$ plane and discard the signal contained within it. A sharp cut-off at the wedge boundary introduces ripples in the estimated $\mathcal{C}_{\ell}^{\text{EP}}(\Delta\nu)$ while performing the Fourier transform (equation 20). In order to avoid this issue, we multiply the $P(k_{\perp}, k_{\parallel})$ with a Butterworth filter of order 16

$$\mathcal{B}(k_{\perp}, k_{\parallel}) = \frac{1}{\sqrt{1 + \left(\frac{r'_c v_c k_{\parallel}}{r_c \sin(\theta_L) k_{\perp}} \right)^{32}}}. \quad (21)$$

The value of the Butterworth function is 1 within wedge and it decays sharply but continuously to zero outside the wedge. The value is $1/\sqrt{2}$ at the wedge boundary. By changing the order of the Butterworth function one can control its steepness and also the amount of foreground spill into the EoR window (Chatterjee, Bharadwaj & Marthi 2019). We then take Fourier transform of $P(k_{\perp}, k_{\parallel}) \mathcal{B}(k_{\perp}, k_{\parallel})$ to get the foreground contaminated $\mathcal{C}_{\ell}^{\text{EP}}(\Delta\nu)$ (equation 20). Finally, we use the ‘Foreground Avoidance’ MAPS $\mathcal{C}_{\ell}^{\text{FA}}(\nu_1, \nu_2) = \mathcal{C}_{\ell}(\nu_1, \nu_2) - \mathcal{C}_{\ell}^{\text{EP}}(\Delta\nu)$ for the MAPS SNR predictions. This leads to subtraction of a part from MAPS at each frequency at any particular ℓ value.

Figs 15 and 16 show the SNR predictions for the diagonal components of MAPS $\Phi^2(\nu, \nu)$ as a function ℓ at $t_{\text{obs}} = 1024$ h for LC1 and LC2, respectively. In these figures, the four panels show the predictions for the ‘Optimistic’, ‘Mild’, ‘Moderate’, and ‘Pessimistic’ scenarios starting from the left to the right, respectively. The first obvious point is that the SNR gradually decreases from the Optimistic to the Pessimistic scenario. This

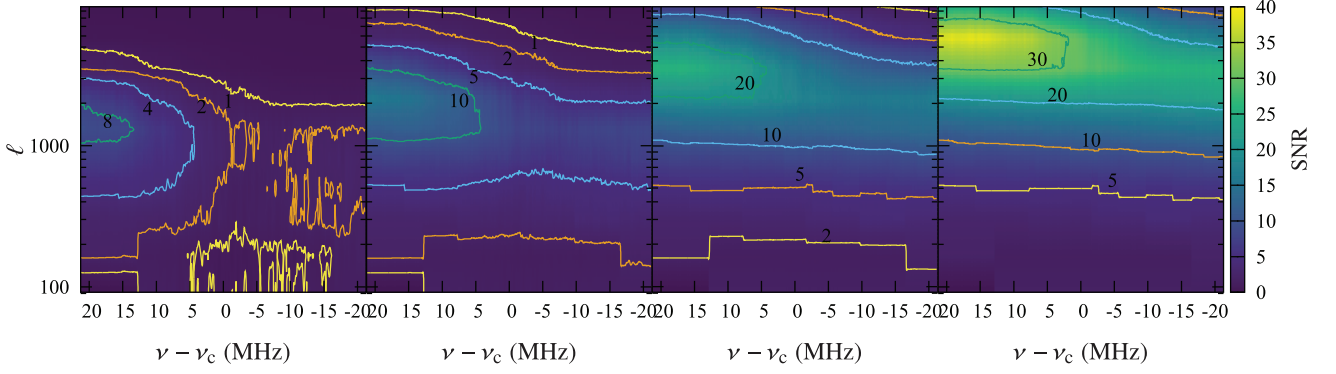


Figure 14. Same as Fig. 13 for the LC2.

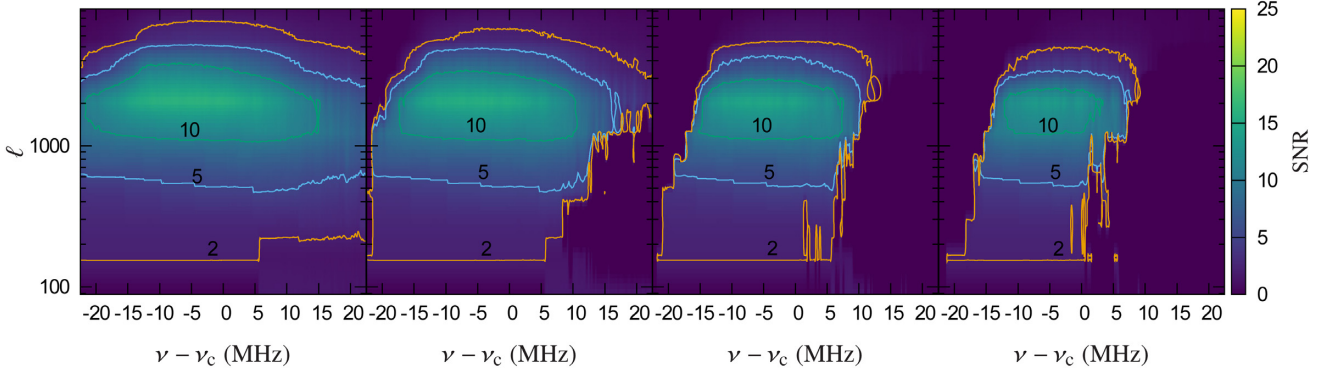


Figure 15. This shows the SNR of the diagonal components of MAPS $\Phi^2(\nu, \nu)$ as a function ℓ at $t_{\text{obs}} = 1024$ h for ‘Optimistic’, ‘Mild’, ‘Moderate’, and ‘Pessimistic’ (from left to right respectively) for the LC1.

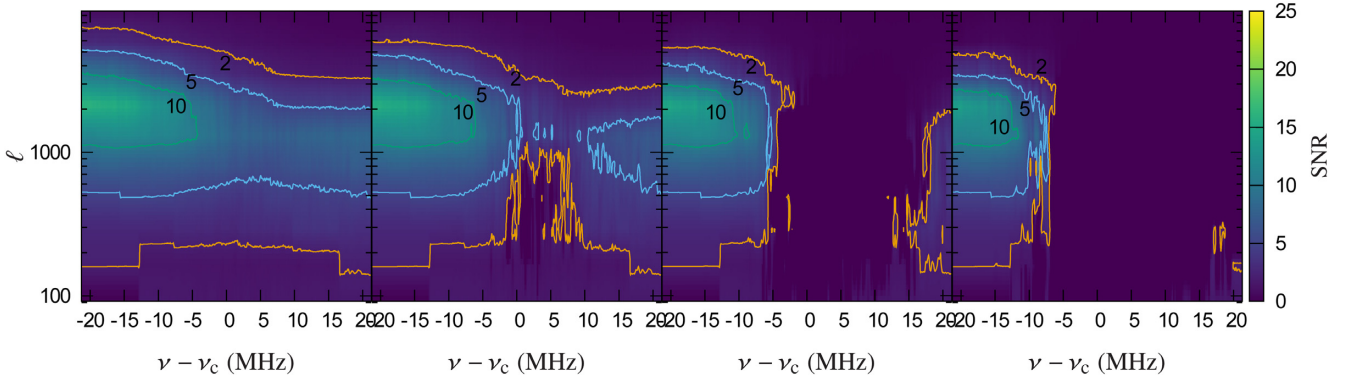


Figure 16. Same as Fig. 15 for the LC2.

happens due to the fact that more number of k_{\parallel} modes are being discarded from the Optimistic to the Pessimistic scenario due to increase in foreground wedge. Note that the extent of the foreground wedge increases at lower ν_c due to the factor $r_c/r'_c \nu_c \sim \sqrt{1420/\nu_c}$ and θ_L as well (Shaw et al. 2019). As a consequence, we see the effects of the foreground wedge is more for LC2 (Fig. 16) as compared to LC1 (Fig. 15). Considering the region where the SNR exceeds the value 5 for LC1, we see the detection of MAPS is possible over the full available bandwidth at $\ell \sim 2000$ for Optimistic scenario. However, the bandwidth for a 5σ detection reduces to ~ 40 , ~ 25 , and ~ 20 MHz for Mild, Moderate, and Pessimistic scenarios, respectively. We find qualitatively similar behaviour in Fig. 16 which shows the results for LC2 simulation. As mentioned above, the impacts of foreground avoidance is more for LC2 box

for being centred at a smaller frequency (higher redshift). Note that this analysis is particularly valid where the signal is ergodic and periodic along the LoS. However, at the moment we do not have a clear picture of how to tackle the foreground problem in the context of MAPS. This is a problem worthy of detailed investigations in future.

7 DISCUSSION AND CONCLUSIONS

Several observational efforts are underway to detect the EoR 21-cm power spectrum $P(k)$ using the presently operating radio interferometers across the globe. One of the key science goals of the future telescope SKA-Low is to measure the spherically averaged

3D EoR power spectrum $P(k)$. The definition of the spherically averaged 3D power spectrum makes use of the assumption that the signal is ergodic and periodic in all three spatial directions. However, the LC effect breaks both ergodicity and periodicity along the LoS of the observer. The problem is particularly severe during EoR where the mean H I fraction \bar{x}_{HI} changes rapidly with redshift and this affects large bandwidth observations with different telescopes (Mondal et al. 2019). The spherically averaged 3D power spectrum $P(k)$ can no longer therefore be regarded as the correct estimator to quantify the second-order statistics of the EoR 21-cm signal (Mondal et al. 2018), and any estimation using this may lead to a biased estimate for the statistics of the signal (Trott 2016). As an alternative to $P(k)$, we have used the MAPS $C_\ell(v_1, v_2)$ to quantify the two-point statistics of the EoR 21-cm signal. This does not assume the signal to be ergodic and periodic along the LoS. The only assumption here is that the signal is statistically homogeneous and isotropic in different directions on the observing plane of the sky. In this work, we make predictions on the SNR for measuring the EoR 21-cm MAPS using the future radio interferometer SKA-Low.

The sensitivity of any instrument to the measurement of the EoR 21-cm MAPS is limited by the errors, a part of which is inherent to the signal itself (cosmic variance), and the other part arises due to the system noise (external contamination). The EoR 21-cm signal is expected to be a highly non-Gaussian field (Bharadwaj & Pandey 2005; Mondal et al. 2015; Majumdar et al. 2018). The effects of this inherent non-Gaussianity play a significant role in the error estimates of the two-point correlation functions of the signal (Mondal et al. 2016, 2017; Shaw et al. 2019). The non-Gaussianity of the signal introduces non-zero trispectrum contribution in the error covariance of the 21-cm MAPS. However in this work, we assume that the observed 21-cm MAPS error covariance is well approximated by that of a Gaussian field predictions and ignored the trispectrum contribution for the simplicity of computations. We have used a 3D radiative transfer code $C^2\text{-RAY}$ to generate the EoR 21-cm LC signal and incorporated observational effects like the system noise and the array baseline distribution to predict the prospects of observing the bin-averaged MAPS using SKA-Low. We have considered two observations **LC1** centred at $\nu_c = 175.58$ MHz, which corresponds to $\bar{x}_{\text{HI}} \approx 0.50$, and **LC2** centred at $\nu_c = 157.08$ MHz, corresponding to $\bar{x}_{\text{HI}} \approx 0.75$. We also present a detailed theoretical framework to quantify and interpret the error estimates for the MAPS incorporating the system noise.

For moderate observation times, we have seen that the rms error σ scales as $1/t_{\text{obs}}$ and consequently we have $\text{SNR} \propto t_{\text{obs}}$. In this case, we have found similar behaviour between the signal and the SNR for MAPS (Figs 4, 5, 9, and 10). They both peak along the diagonal $\nu_1 = \nu_2$ and fall rapidly away from the diagonal. For further analysis, we have focused on the diagonal elements of the MAPS. We have found that the error predictions for MAPS are not much affected by the choice of t_{obs} at large angular scales. This is due to the fact that cosmic variance dominates the total error budget at small ℓ . We have also found that the rms error decreases as t_{obs} is increased at small angular scales. This is because the system noise dominates the total error at large ℓ . We have found that a 5σ detection of MAPS will not be possible with SKA-Low at $\ell \leq 496$ for LC1, and at $\ell \leq 486$ for LC2. Although, we have found that the SKA will be able to measure the MAPS at $\geq 5\sigma$ confidence roughly across the ~ 44 MHz observational bandwidth at $\ell \sim 1300$ with $t_{\text{obs}} \geq 128$ h. Whereas, the frequency band allowed for $\geq 5\sigma$ detection reduces at higher values of ℓ due to system noise domination. We have noted that the rms error increases with decreasing frequency across the bandwidth of our simulations. This is due to the fact that the

system noise contribution increases (equation 8) with decreasing frequency. We have extended our analysis to study how the SNR for the diagonal elements of 21-cm MAPS changes with ℓ (Figs 13 and 14). Note that the system noise contribution, at a fixed ℓ , decreases with as t_{obs} increases but the cosmic variance remains unchanged. However, the cosmic variance dominates the total error at larger values of ℓ for a fixed t_{obs} . This interplay between the system noise and cosmic variance (as a function of t_{obs}) causes the peak of the SNR for MAPS to shift toward larger values of ℓ as t_{obs} is increased (Figs 13 and 14).

In Section 5, we have assumed that the foregrounds are completely removed from the signal. We refer this as the ‘Optimistic’ scenario. In Section 6, we have then attempted to quantitatively address the effects of foregrounds on MAPS detectability forecast. The foreground contamination is found to be restricted within a wedge shaped region in the (k_\perp, k_\parallel) plane (Datta et al. 2010) and the region outside the foreground wedge is utilized for estimating the EoR 21-cm 3D power spectrum $P(k)$ in foreground avoidance technique (Morales et al. 2012; Pober et al. 2013; Kerrigan et al. 2018; Hassan et al. 2019). We have considered three foreground scenarios ‘Mild’, ‘Moderate’, and ‘Pessimistic’ respectively. We have found that the SNR gradually decreases from the Optimistic to the Pessimistic scenario. The bandwidth for a 5σ detection at $\ell \sim 2000$ reduces from full available bandwidth to ~ 40 , ~ 25 , and ~ 20 MHz for Mild, Moderate, and Pessimistic scenarios, respectively for LC1. We have found qualitatively similar behaviour for LC2. However, the impacts of foreground avoidance is more for LC2 for being centred at a smaller frequency (higher redshift).

In conclusion, our study indicates that the EoR 21-cm MAPS, which is directly related to the correlations between the visibilities measured in radio interferometric observation, can be measured at a confidence level of 5σ or more at angular multipole $\ell \sim 1300$ for $t_{\text{obs}} \geq 128$ h across ~ 44 MHz observational bandwidth using SKA-Low. The framework presented in this paper is general and can be applied to any radio interferometer given the array baseline distribution.

ACKNOWLEDGEMENTS

This work was supported by the Science and Technology Facilities Council [grant numbers ST/F002858/1 and ST/I000976/1] and the Southeast Physics Network (SEPNNet). We acknowledge that the results in this paper have been achieved using the PRACE Research Infrastructure resources Curie based at the Très Grand Centre de Calcul (TGCC) operated by CEA near Paris, France and Marenostrum based in the Barcelona Supercomputing Center, Spain. Time on these resources was awarded by PRACE under PRACE4LOFAR grants 2012061089 and 2014102339 as well as under the Multiscale Reionization grants 2014102281 and 2015122822. The authors gratefully acknowledge the Gauss Centre for Supercomputing e.V. (www.gauss-centre.eu) for funding this project by providing computing time through the John von Neumann Institute for Computing (NIC) on the GCS Supercomputer JUWELS at Jülich Supercomputing Centre (JSC). Some of the numerical computations were done on the Apollo cluster at The University of Sussex.

REFERENCES

- Adhikari S., Huterer D., 2019, preprint ([arXiv:1905.02278](https://arxiv.org/abs/1905.02278))
 Ahn K., Iliev I. T., Shapiro P. R., Srisawat C., 2015, *MNRAS*, 450, 1486
 Ali S. S., Bharadwaj S., Chengalur J. N., 2008, *MNRAS*, 385, 2166

- Ali Z. S. et al., 2015, *ApJ*, 809, 61
- Barkana R., Loeb A., 2006, *MNRAS*, 372, L43
- Beardsley A. P. et al., 2013, *MNRAS*, 429, L5
- Becker R. H. et al., 2001, *AJ*, 122, 2850
- Becker G. D., Bolton J. S., Madau P., Pettini M., Ryan-Weber E. V., Venemans B. P., 2015, *MNRAS*, 447, 3402
- Bernardi G. et al., 2009, *A&A*, 500, 965
- Bharadwaj S., Ali S. S., 2005, *MNRAS*, 356, 1519
- Bharadwaj S., Pandey S. K., 2003, *J. Astrophys. Astron.*, 24, 23
- Bharadwaj S., Pandey S. K., 2005, *MNRAS*, 358, 968
- Bharadwaj S., Sethi S. K., 2001, *J. Astrophys. Astron.*, 22, 293
- Bharadwaj S., Pal S., Choudhuri S., Dutta P., 2018, *MNRAS*, 483, 5694
- Bonaldi A., Brown M. L., 2015, *MNRAS*, 447, 1973
- Chatterjee S., Bharadwaj S., 2018, *MNRAS*, 483, 2269
- Chatterjee S., Bharadwaj S., Marthi V. R., 2019, preprint (arXiv:1911.05372)
- Chornock R., Berger E., Fox D. B., Lunnan R., Drout M. R., Fong W.-f., Laskar T., Roth K. C., 2013, *ApJ*, 774, 26
- Choudhuri S., Bharadwaj S., Ghosh A., Ali S. S., 2014, *MNRAS*, 445, 4351
- Choudhuri S., Bharadwaj S., Roy N., Ghosh A., Ali S. S., 2016, *MNRAS*, 459, 151
- Choudhury T. R., Haehnelt M. G., Regan J., 2009, *MNRAS*, 394, 960
- Dai W.-M., Ma Y.-Z., Guo Z.-K., Cai R.-G., 2019, *Phys. Rev. D*, 99, 043524
- Datta K. K., Choudhury T. R., Bharadwaj S., 2007, *MNRAS*, 378, 119
- Datta A., Bowman J. D., Carilli C. L., 2010, *ApJ*, 724, 526
- Datta K. K., Mellema G., Mao Y., Iliev I. T., Shapiro P. R., Ahn K., 2012, *MNRAS*, 424, 1877
- Datta K. K., Jensen H., Majumdar S., Mellema G., Iliev I. T., Mao Y., Shapiro P. R., Ahn K., 2014, *MNRAS*, 442, 1491
- Davies F. B. et al., 2018, *ApJ*, 864, 142
- DeBoer D. R. et al., 2017, *PASP*, 129, 045001
- Dixon K. L., Iliev I. T., Mellema G., Ahn K., Shapiro P. R., 2016, *MNRAS*, 456, 3011
- Ewall-Wice A., Hewitt J., Mesinger A., Dillon J. S., Liu A., Pober J., 2016, *MNRAS*, 458, 2710
- Fan X., Narayanan V. K., Strauss M. A., White R. L., Becker R. H., Pentericci L., Rix H.-W., 2002, *AJ*, 123, 1247
- Fan X. et al., 2006, *AJ*, 132, 117
- Fixsen D. J. et al., 2011, *ApJ*, 734, 5
- Ghosh A., Bharadwaj S., Ali S. S., Chengalur J. N., 2011, *MNRAS*, 418, 2584
- Ghosh A., Prasad J., Bharadwaj S., Ali S. S., Chengalur J. N., 2012, *MNRAS*, 426, 3295
- Giri S. K., Mellema G., Aldheimer T., Dixon K. L., Iliev I. T., 2019, *MNRAS*, 489, 1590
- Greig B., Mesinger A., Haiman Z., Simcoe R. A., 2017, *MNRAS*, 466, 4239
- Greig B., Mesinger A., Bañados E., 2019, *MNRAS*, 484, 5094
- Haiman Z., Holder G. P., 2003, *ApJ*, 595, 1
- Harker G. et al., 2009, *MNRAS*, 397, 1138
- Harnois-Deraps J., Pen U.-L., Iliev I. T., Merz H., Emberson J. D., Desjacques V., 2013, *MNRAS*, 436, 540
- Hassan S., Andrianomena S., Dougherty C., 2019, preprint (arXiv:1907.07787)
- Iliev I. T., Mellema G., Shapiro P. R., Pen U.-L., 2007, *MNRAS*, 376, 534
- Iliev I. T., Mellema G., Shapiro P. R., Pen U.-L., Mao Y., Koda J., Ahn K., 2012, *MNRAS*, 423, 2222
- Jacobs D. C. et al., 2015, *ApJ*, 801, 51
- Jacobs D. C. et al., 2016, *ApJ*, 825, 114
- Kerrigan J. R. et al., 2018, *ApJ*, 864, 131
- Komatsu E. et al., 2011, *ApJS*, 192, 18
- Konno A. et al., 2014, *ApJ*, 797, 16
- Koopmans L. et al., 2015, *Proc. Sci.*, The Cosmic Dawn and Epoch of Reionisation with SKA. SISSA, Trieste, PoS#1
- La Plante P., Battaglia N., Natarajan A., Peterson J. B., Trac H., Cen R., Loeb A., 2014, *ApJ*, 789, 31
- Lidz A., Zahn O., McQuinn M., Zaldarriaga M., Hernquist L., 2008, *ApJ*, 680, 962
- Majumdar S., Pritchard J. R., Mondal R., Watkinson C. A., Bharadwaj S., Mellema G., 2018, *MNRAS*, 476, 4007
- McGreer I. D., Mesinger A., Fan X., 2011, *MNRAS*, 415, 3237
- McGreer I. D., Mesinger A., D'Odorico V., 2015, *MNRAS*, 447, 499
- McQuinn M., Zahn O., Zaldarriaga M., Hernquist L., Furlanetto S. R., 2006, *ApJ*, 653, 815
- McQuinn M., Lidz A., Zahn O., Dutta S., Hernquist L., Zaldarriaga M., 2007, *MNRAS*, 377, 1043
- McQuinn M., Lidz A., Zaldarriaga M., Hernquist L., Dutta S., 2008, *MNRAS*, 388, 1101
- Mellema G., Iliev I. T., Alvarez M. A., Shapiro P. R., 2006, *New Astron.*, 11, 374
- Mellema G. et al., 2013, *Exp. Astron.*, 36, 235
- Mellema G., Koopmans L., Shukla H., Datta K. K., Mesinger A., Majumdar S., 2015, *Proc. Sci.*, HI tomographic imaging of the Cosmic Dawn and Epoch of Reionization with SKA. SISSA, Trieste, PoS#10
- Mertens F. G., Ghosh A., Koopmans L. V. E., 2018, *MNRAS*, 478, 3640
- Mertens F. G. et al., 2020, *MNRAS*, 493, 1662
- Mesinger A., Furlanetto S., Cen R., 2011, *MNRAS*, 411, 955
- Mitra S., Choudhury T. R., Ferrara A., 2015, *MNRAS*, 454, L76
- Mitra S., Choudhury T. R., Ferrara A., 2017, *MNRAS*, 473, 1416
- Mondal R., Bharadwaj S., Majumdar S., Bera A., Acharyya A., 2015, *MNRAS*, 449, L41
- Mondal R., Bharadwaj S., Majumdar S., 2016, *MNRAS*, 456, 1936
- Mondal R., Bharadwaj S., Majumdar S., 2017, *MNRAS*, 464, 2992
- Mondal R., Bharadwaj S., Datta K. K., 2018, *MNRAS*, 474, 1390
- Mondal R., Bharadwaj S., Iliev I. T., Datta K. K., Majumdar S., Shaw A. K., Sarkar A. K., 2019, *MNRAS*, 483, L109
- Morales M. F., 2005, *ApJ*, 619, 678
- Morales M. F., Bowman J. D., Hewitt J. N., 2006, *ApJ*, 648, 767
- Morales M. F., Hazelton B., Sullivan I., Beardsley A., 2012, *ApJ*, 752, 137
- Ota K. et al., 2008, *ApJ*, 677, 12
- Ota K. et al., 2017, *ApJ*, 844, 85
- Ouchi M. et al., 2010, *ApJ*, 723, 869
- Paciga G. et al., 2013, *MNRAS*, 433, 639
- Parsons A. R. et al., 2014, *ApJ*, 788, 106
- Planck Collaboration XIII, 2015, preprint (arXiv:1502.01589)
- Planck Collaboration XLVI, 2016a, *A&A*, 596, A107
- Planck Collaboration XLVII, 2016b, *A&A*, 596, A108
- Pober J. C. et al., 2013, *ApJ*, 768, L36
- Pober J. C. et al., 2014, *ApJ*, 782, 66
- Pober J. C. et al., 2016, *ApJ*, 819, 8
- Robertson B. E. et al., 2013, *ApJ*, 768, 71
- Robertson B. E., Ellis R. S., Furlanetto S. R., Dunlop J. S., 2015, *ApJ*, 802, L19
- Santos S., Sobral D., Matthee J., 2016, *MNRAS*, 463, 1678
- Scott D., Rees M. J., 1990, *MNRAS*, 247, 510
- Shaw A. K., Bharadwaj S., Mondal R., 2019, *MNRAS*, 487, 4951
- Trott C. M., 2016, *MNRAS*, 461, 126
- van Haarlem M. P. et al., 2013, *A&A*, 556, A2
- White M., Carlstrom J. E., Dragovan M., Holzzapfel W. L., 1999, *ApJ*, 514, 12
- Yatawatta S. et al., 2013, *A&A*, 550, A136
- Yoshiura S., Shimabukuro H., Takahashi K., Momose R., Nakanishi H., Imai H., 2015, *MNRAS*, 451, 266
- Zaldarriaga M., Furlanetto S. R., Hernquist L., 2004, *ApJ*, 608, 622
- Zaroubi S. et al., 2012, *MNRAS*, 425, 2964
- Zawada K., Semelin B., Vonlanthen P., Baek S., Revaz Y., 2014, *MNRAS*, 439, 1615
- Zheng Z.-Y. et al., 2017, *ApJ*, 842, L22

APPENDIX A: MAPS ERROR COVARIANCE

The error covariance of the MAPS measured at the i -th and the j -th bins can be written as

$$\begin{aligned} \mathbf{X}_{12,34}^{\ell_i \ell_j'} &= \langle [\hat{C}_{\ell_i}^t(\nu_1, \nu_2) - \bar{C}_{\ell_i}^t(\nu_1, \nu_2)] [\hat{C}_{\ell_j'}^t(\nu_3, \nu_4) - \bar{C}_{\ell_j'}^t(\nu_3, \nu_4)] \rangle \\ &= \langle \hat{C}_{\ell_i}^t(\nu_1, \nu_2) \hat{C}_{\ell_j'}^t(\nu_3, \nu_4) \rangle - \bar{C}_{\ell_i}^t(\nu_1, \nu_2) \bar{C}_{\ell_j'}^t(\nu_3, \nu_4). \end{aligned} \quad (\text{A1})$$

Using equation 11, the first term on the right side of the equation (A1) can be expressed as

$$\begin{aligned} \langle \hat{C}_{\ell_i}^t(\nu_1, \nu_2) \hat{C}_{\ell_j'}^t(\nu_3, \nu_4) \rangle &= \frac{1}{4\Omega^2} \sum_{\mathbf{U}} \sum_{\mathbf{U}'} w(\mathbf{U}) w(\mathbf{U}') \\ &\times [\langle \tilde{T}_{b_2}^t(\mathbf{U}, \nu_1) \tilde{T}_{b_2}^t(-\mathbf{U}, \nu_2) \tilde{T}_{b_2}^t(\mathbf{U}', \nu_3) \tilde{T}_{b_2}^t(-\mathbf{U}', \nu_4) \rangle \\ &+ \langle \tilde{T}_{b_2}^t(\mathbf{U}, \nu_1) \tilde{T}_{b_2}^t(-\mathbf{U}, \nu_2) \tilde{T}_{b_2}^t(-\mathbf{U}', \nu_3) \tilde{T}_{b_2}^t(\mathbf{U}', \nu_4) \rangle \\ &+ \langle \tilde{T}_{b_2}^t(-\mathbf{U}, \nu_1) \tilde{T}_{b_2}^t(\mathbf{U}, \nu_2) \tilde{T}_{b_2}^t(\mathbf{U}', \nu_3) \tilde{T}_{b_2}^t(-\mathbf{U}', \nu_4) \rangle \\ &+ \langle \tilde{T}_{b_2}^t(-\mathbf{U}, \nu_1) \tilde{T}_{b_2}^t(\mathbf{U}, \nu_2) \tilde{T}_{b_2}^t(-\mathbf{U}', \nu_3) \tilde{T}_{b_2}^t(\mathbf{U}', \nu_4) \rangle]. \end{aligned} \quad (\text{A2})$$

Using $\tilde{T}_{b_2}^t(\mathbf{U}, \nu) = \tilde{T}_{b_2}(\mathbf{U}, \nu) + \tilde{T}_{b_2}^N(\mathbf{U}, \nu)$ and equation 7, the first ensemble average in equation (A2) can be arranged as

$$\begin{aligned} \langle \tilde{T}_{b_2}^t(\mathbf{U}, \nu_1) \tilde{T}_{b_2}^t(-\mathbf{U}, \nu_2) \tilde{T}_{b_2}^t(\mathbf{U}', \nu_3) \tilde{T}_{b_2}^t(-\mathbf{U}', \nu_4) \rangle &= \Omega^2 [\{C_{\ell}(\nu_1, \nu_2) C_{\ell'}(\nu_3, \nu_4) + \delta_{\nu_3 \nu_4}^K C_{\ell}(\nu_1, \nu_2) C_{\ell'}^N(\nu_3, \nu_4) \\ &+ \delta_{\nu_1 \nu_2}^K C_{\ell}^N(\nu_1, \nu_2) C_{\ell'}(\nu_3, \nu_4) + \delta_{\nu_1 \nu_2}^K \delta_{\nu_3 \nu_4}^K C_{\ell}^N(\nu_1, \nu_2) C_{\ell'}^N(\nu_3, \nu_4)\} \\ &+ \delta_{\mathbf{U}-\mathbf{U}', 0}^K \{C_{\ell}(\nu_1, \nu_4) C_{\ell'}(\nu_2, \nu_3) + \delta_{\nu_2 \nu_3}^K C_{\ell}(\nu_1, \nu_4) C_{\ell'}^N(\nu_2, \nu_3) \\ &+ \delta_{\nu_1 \nu_4}^K C_{\ell}^N(\nu_1, \nu_4) C_{\ell'}(\nu_2, \nu_3) + \delta_{\nu_1 \nu_4}^K \delta_{\nu_2 \nu_3}^K C_{\ell}^N(\nu_1, \nu_4) C_{\ell'}^N(\nu_2, \nu_3)\} \\ &+ \delta_{\mathbf{U}+\mathbf{U}', 0}^K \{C_{\ell}(\nu_1, \nu_3) C_{\ell'}(\nu_2, \nu_4) + \delta_{\nu_2 \nu_4}^K C_{\ell}(\nu_1, \nu_3) C_{\ell'}^N(\nu_2, \nu_4) \\ &+ \delta_{\nu_1 \nu_3}^K C_{\ell}^N(\nu_1, \nu_3) C_{\ell'}(\nu_2, \nu_4) + \delta_{\nu_1 \nu_3}^K \delta_{\nu_2 \nu_4}^K C_{\ell}^N(\nu_1, \nu_3) C_{\ell'}^N(\nu_2, \nu_4)\}], \end{aligned} \quad (\text{A3})$$

where $\delta_{\mathbf{U}-\mathbf{U}', 0}^K$ and $\delta_{\mathbf{U}+\mathbf{U}', 0}^K$ are Kronecker's delta. Here, we have considered that $\tilde{T}_{b_2}(\mathbf{U}, \nu)$ correlates at same baselines \mathbf{U} and

$\tilde{T}_{b_2}^N(\mathbf{U}, \nu)$ correlates at same \mathbf{U} and same frequency ν . We obtain this expression after ignoring the non-Gaussianity of the EoR 21-cm signal. However, the inherent non-Gaussianity gives rise to a non-zero four point connected term (trispectrum; see equation 2 of Adhikari & Huterer 2019) in the cosmic variance of MAPS. The non-zero trispectra will introduce additional term in equation (A3) which will eventually increase the variance and also introduce correlations between errors in the estimated MAPS. We finally ignore trispectrum contribution in our error analysis following the discussion in Section 4.2.

The MAPS estimations are restricted to the upper half of the baseline distribution. Hence, $\delta_{\mathbf{U}+\mathbf{U}', 0}^K = 0$ and equation A3 reduces to

$$\begin{aligned} \langle \tilde{T}_{b_2}^t(\mathbf{U}, \nu_1) \tilde{T}_{b_2}^t(-\mathbf{U}, \nu_2) \tilde{T}_{b_2}^t(\mathbf{U}', \nu_3) \tilde{T}_{b_2}^t(-\mathbf{U}', \nu_4) \rangle &= \Omega^2 [C_{\ell}^t(\nu_1, \nu_2) C_{\ell'}^t(\nu_3, \nu_4) + \delta_{\mathbf{U}-\mathbf{U}', 0}^K C_{\ell}^t(\nu_1, \nu_4) C_{\ell'}^t(\nu_2, \nu_3)]. \end{aligned} \quad (\text{A4})$$

Similarly, one can write down the other three ensemble averages of equation (A2) by permuting the frequency indices in equation (A4). Combining equation (A1) and (A4) with the other ensemble averages, we write the error covariance in compact form

$$\begin{aligned} \mathbf{X}_{12,34}^{\ell_i \ell_j'} &= \frac{1}{2} \delta_{\mathbf{U}-\mathbf{U}', 0}^K \sum_{\mathbf{U}} \sum_{\mathbf{U}'} w(\mathbf{U}) w(\mathbf{U}') [C_{\ell_i}^t(\nu_1, \nu_3) C_{\ell_j'}^t(\nu_2, \nu_4) \\ &+ C_{\ell_i}^t(\nu_1, \nu_4) C_{\ell_j'}^t(\nu_2, \nu_3)]. \end{aligned} \quad (\text{A5})$$

Finally, exploiting the Kronecker's delta, we obtain

$$\mathbf{X}_{12,34}^{\ell_i} = \frac{1}{2} \sum_{\mathbf{U}} w^2 [C_{\ell}^t(\nu_1, \nu_3) C_{\ell}^t(\nu_2, \nu_4) + C_{\ell}^t(\nu_1, \nu_4) C_{\ell}^t(\nu_2, \nu_3)]. \quad (\text{A6})$$

This paper has been typeset from a $\text{\TeX}/\text{\LaTeX}$ file prepared by the author.